QUANTITATIVE ANALYSIS OF TOMOGRAPHIC IMAGING FOR MULTIPHASE FIELDS
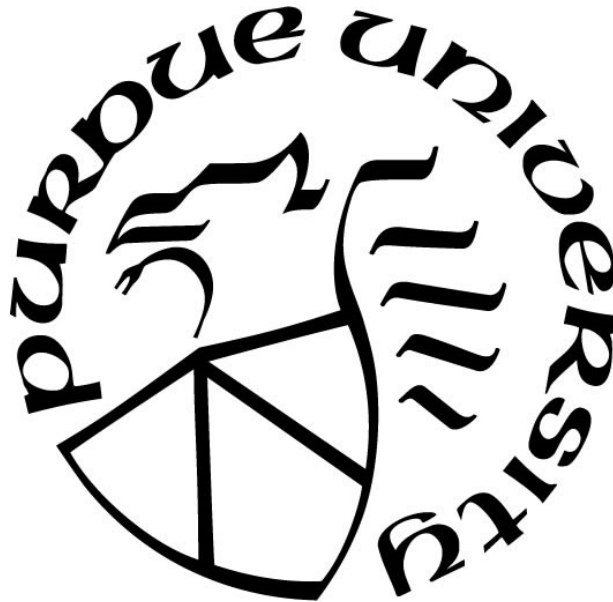
by

Deepti Gnanaseelan

A Thesis

Submitted to the Faculty of Purdue University

In Partial Fulfillment of the Requirements for the degree of

Master of Science in Mechanical Engineering

School of Mechanical Engineering

West Lafayette, Indiana

August 2020

THE PURDUE UNIVERSITY GRADUATE SCHOOL
STATEMENT OF COMMITTEE APPROVAL

Dr. Terrence Meyer, Chair

School of Mechanical Engineering

Dr. Mikhail Slipchenko

School of Mechanical Engineering

Dr. Paul Sojka

School of Mechanical Engineering

Approved by:

Dr. Nicole Key

Dedicated to my parents

ACKNOWLEDGMENTS

First and foremost, I would like to thank my professor, Dr. Terrence Meyer, for giving me the opportunity to pursue my MS thesis under his guidance. It has been a truly memorable experience working under the guidance of someone as knowledgeable, supportive and helpful as him.

I would also like to thank Dr. Mikhail Slipchenko for his support and guidance throughout these two years. I would also like to express my sincere gratitude to Dr. Slipchenko and Dr. Sojka for gracing my graduate committee.

I would like to express my sincere gratitude to my mentor, Venkat Athmanathan, for guiding me through the initial phase of my transition as a graduate student at Purdue. I would also like to thank Daniel Lauriola, Mateo Gomez, Naveed Rahman, and Josh Ludwigsen for their guidance and help with setting up my experiments and processing my data. I am also grateful to Austin, Amanda, Mike, Matt, Jeremy, Jon, Zac, Eric, Alex, and Jordan for their guidance during the last two years. I was fortunate to have been a part of a wonderful and immensely supportive lab group.

I would like to thank my parents and family members for their constant guidance and encouragement without which I wouldn't be here today. I am who I am today because of the stable pillars of strength that they have always been in my life.

I would also like to express my heartfelt thanks to Hrishikesh for his unconditional support.

Last but not the least, a big thank you to Radhika, Rashmi, and Siddhant for being my constants, especially during the final stages of this thesis.

Each and every one of you have been instrumental in making my journey at Purdue memorable and I couldn't have done this without all of you.

TABLE OF CONTENTS

LIST OF TABLES

LIST OF FIGURES

9

LIST OF ABBREVIATIONS

DIH   Digital Inline Holography

LII   Laser Induced Incandescence

MART   Multiplicative Algebraic Reconstruction Technique

PLIF   Planar Laser Induced Fluorescence

SLIPI   Structured Laser Induced Planar Imaging

SMD   Sauter Mean Diameter

WARP   Wide-Angle Relay Plenoptic

ABSTRACT

Multiphase fields find wide applications in the fields of combustion, sprays, turbomachinery, heating and cooling systems, blasts, energetic materials, and several more areas of engineering interest. As the efficiency and performance of these systems depend heavily on the underlying multiphase field, studying their intricate structural features becomes important. The current study follows the development of a three-dimensional Wide-Angle Relay Plenoptic (WARP) imaging system with two image quadruplers for the tomographic imaging of multiphase fields. 3D printed targets were used to simulate both semi-transparent as well as opaque particle fields to emulate multiphase systems. Tomographic reconstruction of the targets was performed using the iterative MART reconstruction algorithm in a commercial image processing software. Reconstructions were performed at different angular separations between the cameras as well as for varied separation distance between the object and the imaging system. Quantitative analysis of the reconstruction quality of the developed system was performed to study the effectiveness and accuracy of this system in imaging multiphase fields. The effect of varying different system parameters on reconstruction quality has been studied to evaluate the best system configuration for imaging multiphase fields.

1. INTRODUCTION

1.1 Background

Multiphase systems generally refer to systems involving the presence of two or more phases or components [1]. Such systems find wide applications in the fields of combustion, flow systems, explosions, turbomachinery, spraying systems, material properties, and a variety of different domains. To ensure the efficiency and effectiveness of all these processes, it becomes essential to predict the behavior of these systems. One of the most important characteristics of these systems is the phase separation. Understanding the separation layer between phases, the phase distribution, and the corresponding structures of the different phases enable engineers and researchers to design better and more efficient systems. Researchers have worked on obtaining two-dimensional images at different orientations and planar slices through the field to delve deeper into these structures and their implications on different applications through studies based on light scattering, laser techniques [Planar Laser Induced Fluorescence (PLIF), Laser Induced Incandescence (LII)], Shadowgraphy, and so on. With an increased interest to understand the three-dimensional nature of these structures, research has been carried forward in areas like holography, X-ray imaging, tomographic imaging, volumetric LIF and LII, and computed tomography. More recently, four-dimensional imaging (three spatial directions and time) studies have also been attempted with the use of high-speed cameras which can capture time varying trends of the volume under consideration.

Most volumetric reconstruction studies require the use of multiple views from varied angles to ensure a good reconstruction. A good volumetric reconstruction dictates the use of more than four views (ideally about eight preferred) [2], to adequately capture all necessary features within the system under study. This can be accomplished using an equal number of cameras, although potentially with a high system cost. To limit the number of cameras, work has been done to allow multiple images to be captured on the same camera. This utilizes a stereoscope which allows two views to be captured using a single camera requiring half the number of cameras [2]–[4]. Another alternative is the use of a quadscope, an image quadrupler, which allows four views to be captured with the help of a single camera [5]–[7], reducing the number of cameras by a factor of four. This method is called Wide-Angle Relay Plenoptic (WARP) imaging and the resulting use

of fewer optics causes significant reduction in experimentation costs. However, this compromises the spatial resolution, that is the number of camera pixels that comprises a particular camera view.

The use of a WARP system in tomographic imaging and the quality of the subsequent reconstruction of multiphase fields for up to eight views has been studied as a part of this work.

1.2   Importance of Multiphase Fields

Multiphase systems may either be dispersed, wherein one phase exists as finite particles within a continuous second phase; separated, wherein two or more continuous phases coexist separated by simple geometrical interfaces; or mixed, wherein there is a transition between separated and dispersed [8]. It may refer to gas/solid flows, liquid/solid flows, bubbly flows, slurries, aerosols, fluidized beds, and so on. Some common multiphase fields have been detailed in this section, along with implications for imaging systems.

1.2.1   Sprays

One of the most common liquid/gas multiphase flows is a spray. A spray is a collection of liquid drops dispersed within a fluid, generally air. It is formed when the interface between a liquid and a gas become deformed and droplets of liquid are generated [1]. The structure of a spray determines the combustion efficiency and the exhaust emissions from internal combustion engines. Similarly, it is also important in liquid-jet machining, inkjet and 3D printing, industrial spray coating, materials synthesis, and a multitude of other natural as well as engineering applications [9]. They also range in scale from the large global air-sea interaction, spillways, and plunge pools to the much smaller fuel injection systems and ink jet systems. They undergo different stages in their breakdown process from a steady stream to ligaments and finally droplets, which further undergo breakup through various mechanisms. Hence, developing a method to visualize and measure all these structures gains great importance, especially due to the widely variant mechanisms involved in their production. Over the past many years, researchers have developed many two-dimensional and, more recently, three-dimensional techniques for better visualization of these different characteristics. The technique used varies greatly with the specific spray under study [10] as the spray density, breakup regime, and presence of structures offer significant influence on the same.

The atomization process is one in which bulk liquid is converted into small drops. A jet or sheet of liquid undergoes different atomization processes to form droplets based on the liquid properties and flow conditions. The larger droplets formed from this primary atomization could further undergo secondary atomization to form smaller drops. The final spray structure is a culmination of all these put together. Several researchers have worked on studying the different breakup modes for sprays as well as the effect of flow velocity, Weber number (a dimensionless quantity that measures the relative importance of a fluid's inertia to its surface tension), fluid viscosity, Reynolds number (ratio of inertial to viscous forces), and so on [11]–[14]. Figure 1 shows the different breakup regimes for a circular liquid jet in quiescent air. The effect of Weber number is clearly visible on the stream.

It is clear that the liquid breakup process leads to a wide range of spatial scales, and it is important to study macroscale phenomena prior to reaching full droplet atomization. This requires the use of illumination and imaging methods that can resolve optically complex multiphase flow structures.
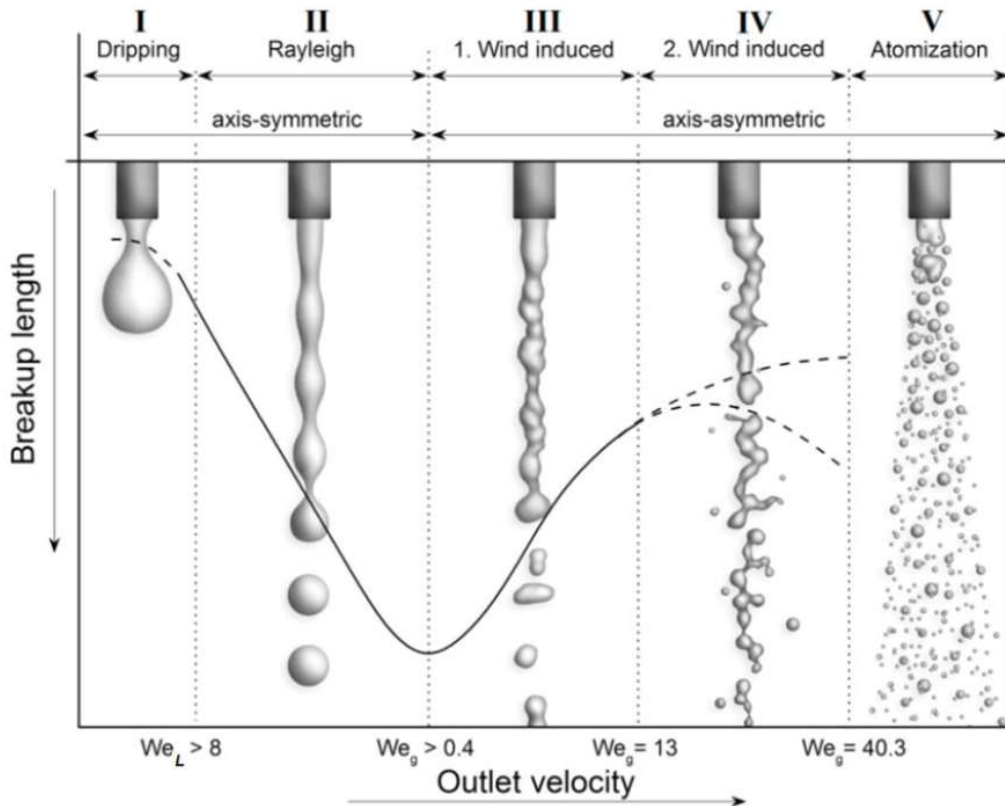
Figure 1. Breakup regimes for round liquid jets in quiescent air [15]

1.2.2 Cavitation

Cavitation is the phenomenon wherein rapid pressure changes in a fluid causes small vapor filled cavities (bubbles) to form in regions of relatively lower pressure. When these bubbles are subjected to higher pressure, they collapse and can generate localized shock waves which could cause serious structural damage to turbines and pumps. It is very common in turbomachinery and the tendency increases with an increase in power. It erodes machine parts, deteriorates machine performance, causes noise, vibrations and oscillations in the entire system, and also enhances corrosion and silt erosion in the metallic parts [16]. To ensure cavitation free design, it is essential to study the flow characteristics and optimize the design to either ensure no sudden pressure surges or combat the bubbles before any structural damage. Figure 2 shows the typical erosion of a turbine blade due to cavitation. While not the focus of this study, it may also be of interest to study the gas-liquid interface of cavitation bubbles using tomography, depending on the range of size scales.
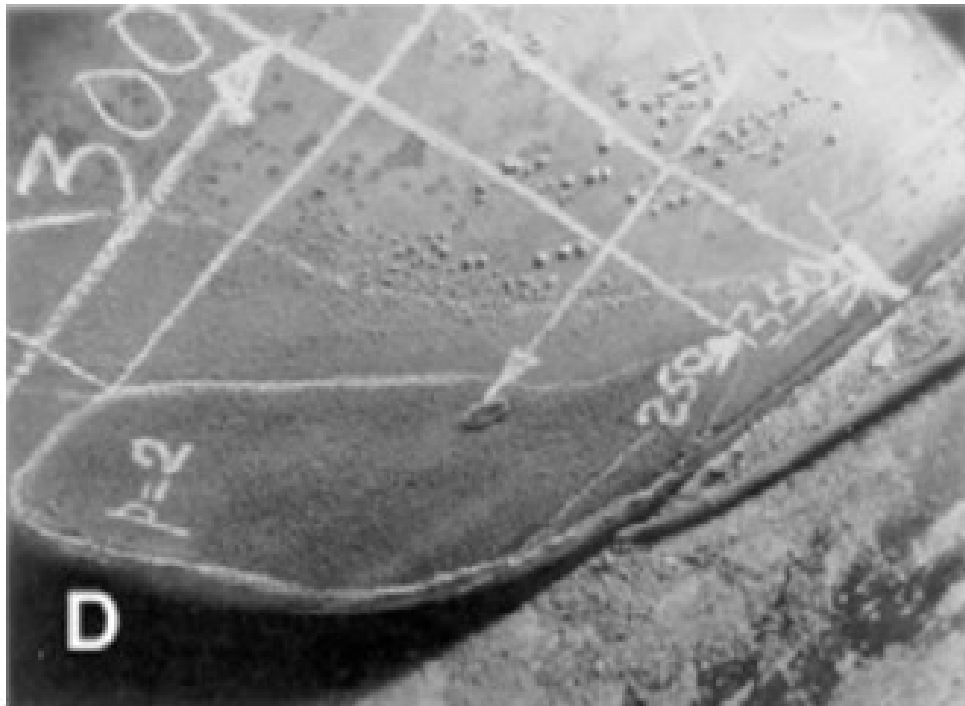
Figure 2. Typical erosion at the suction side of a turbine blade due to cavitation [17]

1.2.3 Evaporation

Evaporation is a process in which a substance transforms from its liquid phase to its vapor phase by the external application of heat. The evaporation process, hence, is also a multiphase process as two different phases of the same substance coexist at the same time. Evaporation processes are very important to study as they dictate combustion efficiency in internal combustion engines, cooling rates in cooling systems, drying rates in heated drying applications, crystal formation, and many other critical applications. The evaporation process is affected by drop/jet size, ambient temperature and pressure, and flow behavior [18]–[21]. Complete understanding of the evaporation process will be highly useful in ensuring more efficient systems. Figure 3 shows the evaporation of a liquid drop, caused due to a heated nitrogen crossflow. The motion of the vapor away from the drop region is clearly visible. In the current work, the focus is on the condensed phase, although it is clear that complex liquid-vapor processes may also be of interest.

(a)   (b)
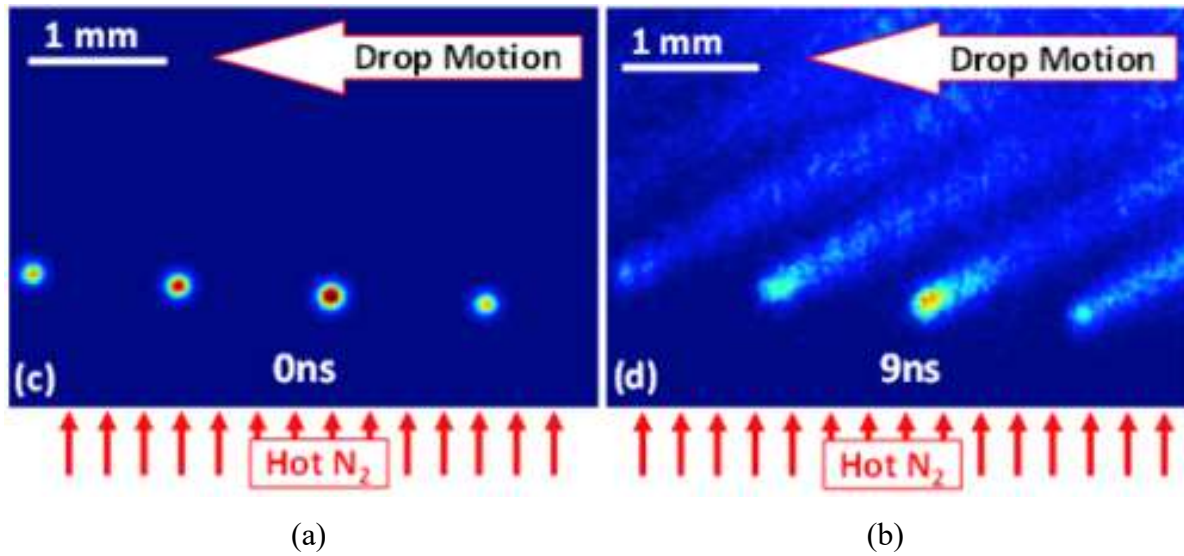
Figure 3. Evaporation of a liquid drop in heated nitrogen crossflow captured using PLIF imaging (a) Image of the liquid drop; (b) Image of the evaporated vapor from the drop (taken 9 ns after the first image) [20]

1.2.4 Combustion

Combustion is an exothermic redox reaction in which a fuel reacts with an oxidizer (generally oxygen) to produce oxidized products. Combustion powers majority of our

transportation systems, energy generation plants, metal refineries, heat treating furnaces, and many other industries. Combustion processes are highly multicomponent, and a study of its constituent products and their distribution is essential for good combustion design, as well as designing any aftertreatment systems as need be.

Combustion involves a series of chemical reactions and is not necessarily a single step process. The reactions steps involved in combustion form an area of great research interest [22]–[24]. Similarly, finding the location and presence of different combustion radicals is a field of many research studies [2], [25]–[27]. The performance of ignition systems, injection systems for fuel sprays, and combustion system designs may all be verified and tested through these methods. Pollution is another major issue due to combustion and may also be tackled using a similar approach. Studying the combustion process is essential in the development of new and efficient engines, finding new alternative fuels, and ensuring safe design. Figure 4 shows an image of a swirl-stabilized flame for JP-8 jet fuel. PLIF has been used to image both the fuel and OH radical regions while LII has been used to capture the soot formed. The effect of each additional diagnostic is clearly visible in the images. The use of three-dimensional tomography has already been evaluated for vapor fields, but the reconstruction of the liquid phase requires further investigation.
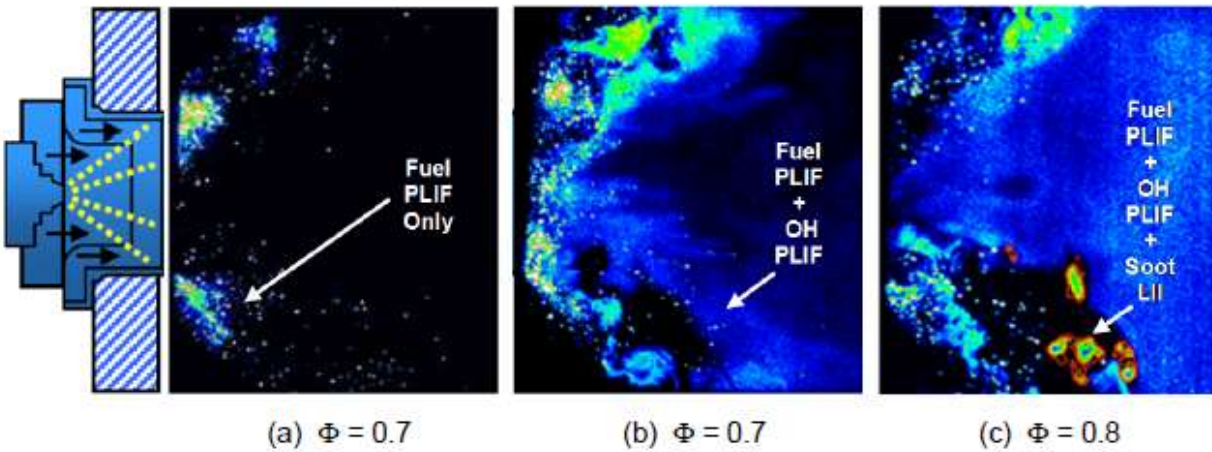
Figure 4. Laser diagnostics being used in a swirl-stabilized flame fueled by JP-8 showing (a) fuel PLIF; (b) fuel PLIF and OH PLIF; and (c) fuel PLIF, OH PLIF, and soot incandescence [10]

1.2.5 Blasts and Explosions

Explosions result in rapid increase in volume and release of energy with generation of high temperatures and release of gases. Explosions are generally accompanied by shock waves as well as the rapid motion of solid particles due to the force of the explosion and fragmentation from the explosive. The motion of the blast wave and the solid particles all result in a resultant multiphase field. Study of blast waves and the trajectories of the fragmented particles find a lot of defense and engineering applications. The diagnosis of blast waves has been studied by several researchers and is still an ongoing field of study [7], [28]–[30]. Figure 5 shows the sequence of images captured near the muzzle of a submachine gun after a gunshot. Of interest in this work is the potential for reconstructing solid phase fields such as those found in fragmenting particles.
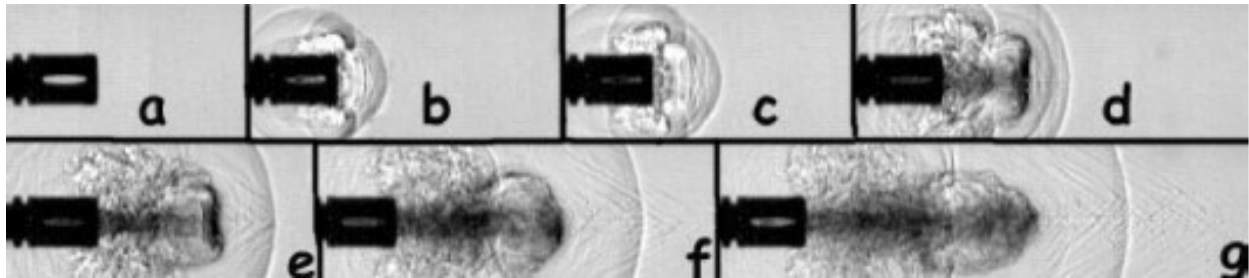
Figure 5. Sequence of frames from a 9mm submachine gun fire observed using shadowgraphy [30]

1.3 Optical Imaging Techniques

Over the years several imaging techniques have been used to image both external as well as cross-sectional features of flows. Some commonly used optical imaging techniques are discussed in this section.

1.3.1 Planar Laser Induced Fluorescence

PLIF is a technique in which a laser light sheet is used to illuminate a substance under study and the substance re-emits a part of the incident light at a longer wavelength. The biggest advantages of using this technique are the high intensity with which this phenomenon of fluorescence occurs, the property of this intensity being directly proportional to the concentration of the species under study, and the fact that the re-emitted signal has a higher wavelength than the incident radiation. In addition, non-fluorescing substances may also be studied with the use of a

fluorescent tracer combination having a monomer (M) and a ground-state molecule (G). This method is called Planar Laser Induced Exciplex Fluorescence (PLIEF or PLIXF). The unique aspect of this method is that on excitation with a laser, the monomer forms an excited monomer (M*). If M* collides with G, a loosely bound complex of the two, called an exciplex (E*) is formed. As the possibility of this collision is much higher in the liquid phase than the vapor phase, it is seen that E* is generally found in the liquid phase while M* is found in the vapor phase. As some amount of energy is spent in the production of E*, it is seen that the fluorescence signal from E* is further red shifted from that of M*. This property helps to distinguish between the vapor and liquid phases of the spray, which is extremely important to understand the liquid and vapor concentrations for a given spray. For a fuel spray, this forms a means to obtain information about the fuel phase distribution within the region of interest (cylinder) after injection, the mixing behavior in the combustion chamber, the evaporation characteristics of the spray, and so on, all of which help to understand and improve combustion processes and hence emission control. Hence, this makes this method extremely useful in spray diagnostics.

Since its first use to study fuel drops and vapor [31], PLIF has been utilized by several researchers to study a variety of sprays [4], [32]–[34]. In combustion, it has been used to image fuel particles as well as radicals like OH and CH. It has also been used to image liquid and vapor regions in evaporating sprays [20], [35]–[37]. An example of the same is seen in Figure 6. Because of the three-dimensional nature of the flow distribution, planar imaging is not able to capture the full evolution of the spray structure.
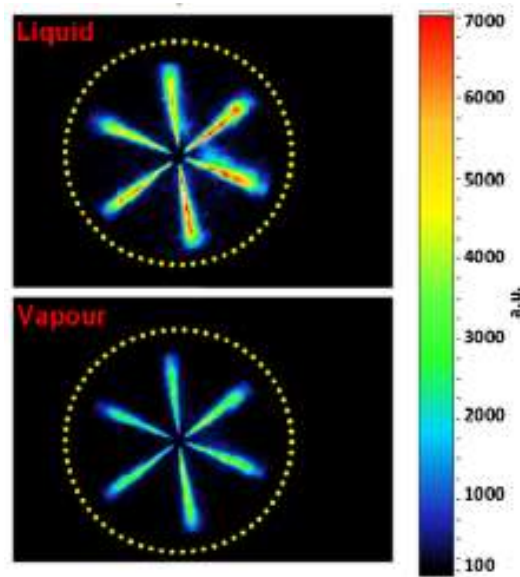
Figure 6. Spatial distribution of liquid and vapor phases for an evaporating diesel spray from a multi-hole nozzle [38]

Recently, researchers have started using laser light to illuminate a target volume and then perform PLIF studies with multiple cameras at different angles and perform tomographic reconstructions, in a method called volumetric laser induced fluorescence or v-LIF [6], [39] but these studies have so far been limited to combustion diagnostics and aerosol fields. For example, Figure 7 shows the application of v-LIF to a laminar flame. Part (a) shows the raw images captured by four cameras with image doublers. Part (b) shows a half section of the reconstructed flame while a projection of the top view of the entire reconstructed flame along the y-axis is provided in part (c). There is a lot of potential for the use of v-LIF for studying polydisperse multiphase fields.
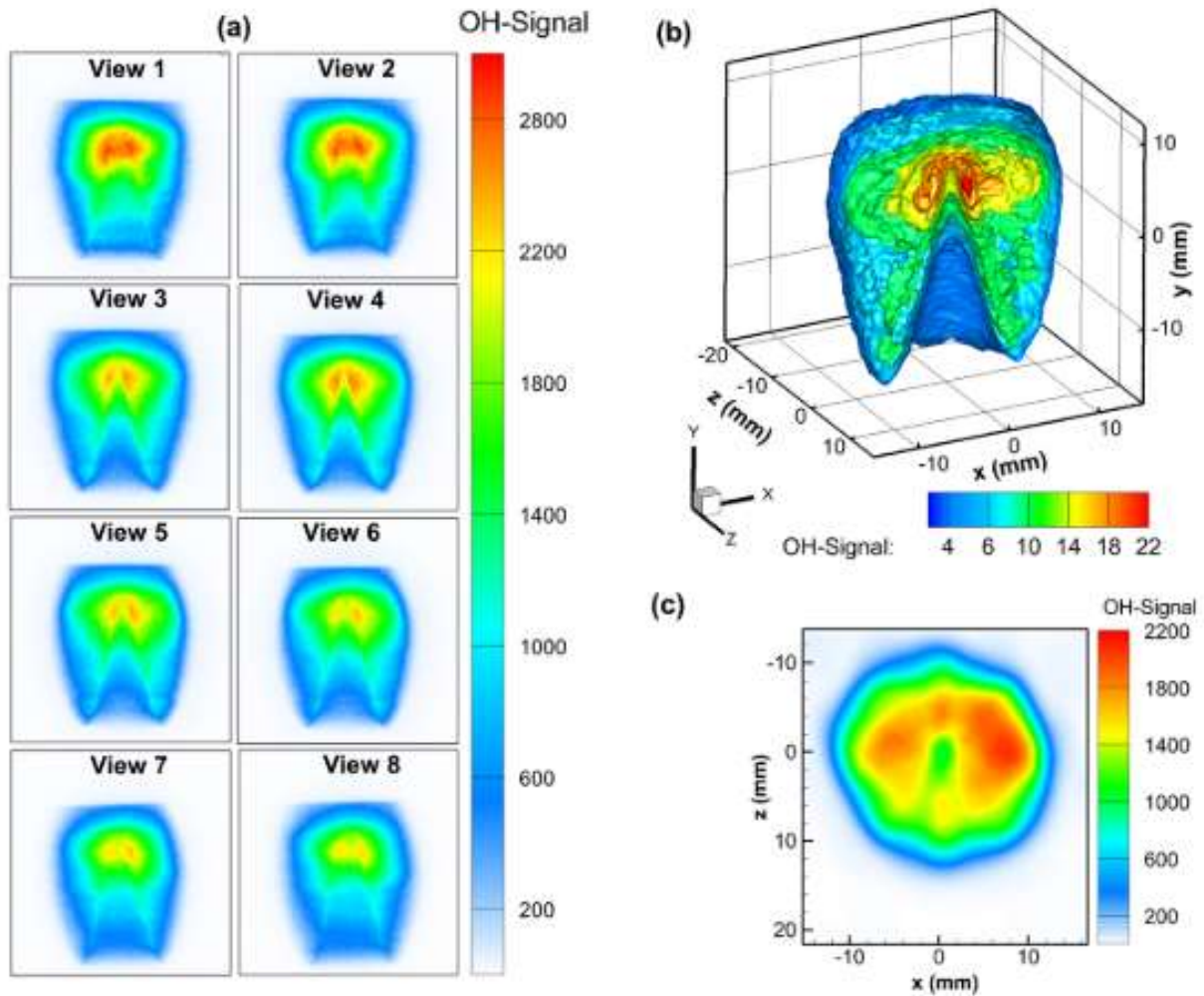
Figure 7. (a) Raw images of OH fluorescence from a laminar flame, captured simultaneously by four cameras with image splitters. (b) Corresponding single-shot tomographic reconstruction of half of the volume. (c) Top view projection of entire reconstructed volume [40]

1.3.2 Planar Mie Scattering

Mie scattering refers to the elastic scattering of light by particles with sizes on the order of or larger than the wavelength of incident light. The signal from Mie scattering is proportional to the square of the particle diameter and depends on individual particles. Mie scattering intensity can be used as a direct measure of the surface area of droplets [10]. Generally, visible light is used to ensure that no fluorescence is induced in the field under study. For illumination, a laser sheet having a thickness of less than 1 mm is formed to slice the spray at the desired plane to be imaged.

Mie scattering has wide application in spray visualization. Studies have been done wherein Mie scattering is used either alone [41], [42] or in conjugation with LIF imaging [43], [44]. The LIF/Mie scattering considers that the LIF signal is directly proportional to the volume and the Mie signal is directly proportional to the surface area. Hence, after careful calibration, the direct ratio of these signals can give the SMD of the droplets in the field [45]. However, conventional LIF/Mie scattering is seen to be affected by errors due to multiple light scattering.

In order to avoid this, Berrocal *et al* [46] developed a system which combined structured illumination with laser imaging (SLIPI). In this technique, the singly scattered light contains a modulated pattern signature which is lost in the multiply scattered light. The undisturbed modulated component (AC component) of light then faithfully represents the singly scattered light while the multiply scattered light will be dominated by the non-modulated signature [45], [46]. The information about the singly scattered light may then be separated by extracting the amplitude of the modulation. Figure 8 shows the improvement in the SMD distribution for the drops from the spray with the use of SLIPI LIF/Mie as opposed to conventional LIF/Mie. The reduction in blurring and smoothing is evident in the case of SLIPI LIF/Mie.

Despite the benefits of using the SLIPI technique to measure drop size, its use is limited to two-dimensional fields as of now. However, it is potentially very useful in three-dimensional fields for the measurement of SMD as well. Figure 8 shows the averaged images for both conventional as well as SLIPI LIF/Mie imaging.
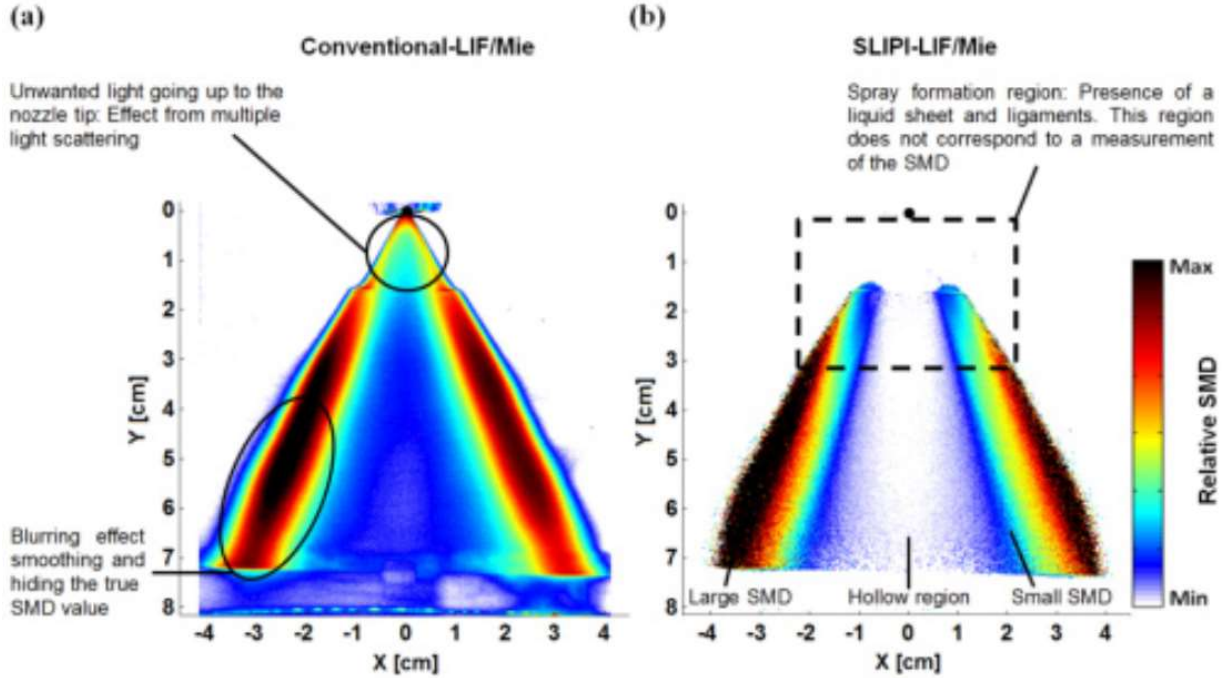
Figure 8. Averaged image of (a) Conventional LIF/Mie, and (b) SLIPI LIF/Mie, representing the relative SMD of the droplet distribution [45]

1.3.3 Shadowgraphy and Ballistic Imaging

Shadowgraphy is an optical method that reveals non-uniformities in transparent media due to a resulting change in the refractive index of the field. It is useful in fields having temperature gradients, multicomponent compositions and shock waves, all of which show these refractive index variations. As the light ray is diffracted away by a difference in density, that point on the detector where the undeflected ray would have arrived, remains dark. The position where the deflected ray arrives, however, appears brighter than the undisturbed environment. The resulting image is called a shadowgraph. Shadowgraph studies have been widely used for the study of sprays and shockwaves [30], [47]–[49]. Figure 9 shows a shadowgraph for a spray while a shadowgraph for a gunshot is shown in Figure 5.
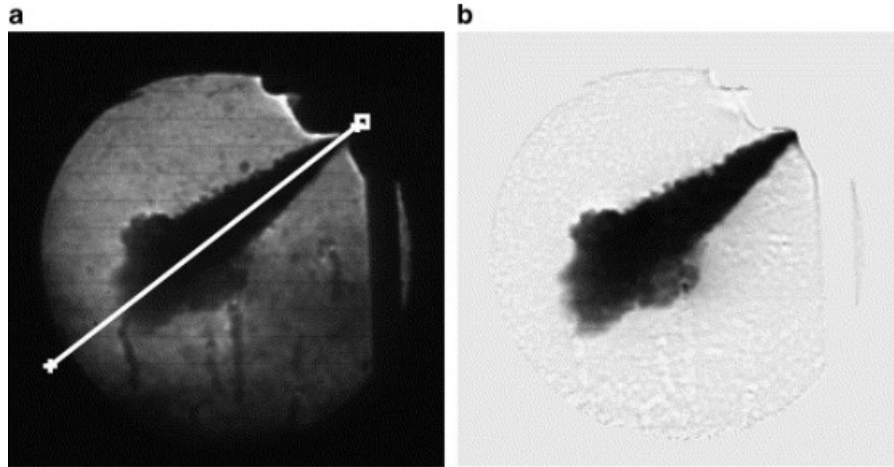
Figure 9. (a) Unprocessed spray shadow image; (b) Illumination corrected image of (a) [47]

Figure 10 shows a comparative study between PLIF, Mie scattering, and shadowgraphy, as applied to a spray. Both LIF and Mie were able to show the internal non-homogeneities of the liquid spray while shadowgraphy was unable to distinguish this and gave homogeneous readings for the same. Moreover, they showed the formation of a high-density homogeneous core followed by a surface disturbance which causes a repeatable stripe shaped structure of lower and higher concentration regions in the liquid bulk.

(a)   (b)   (c)
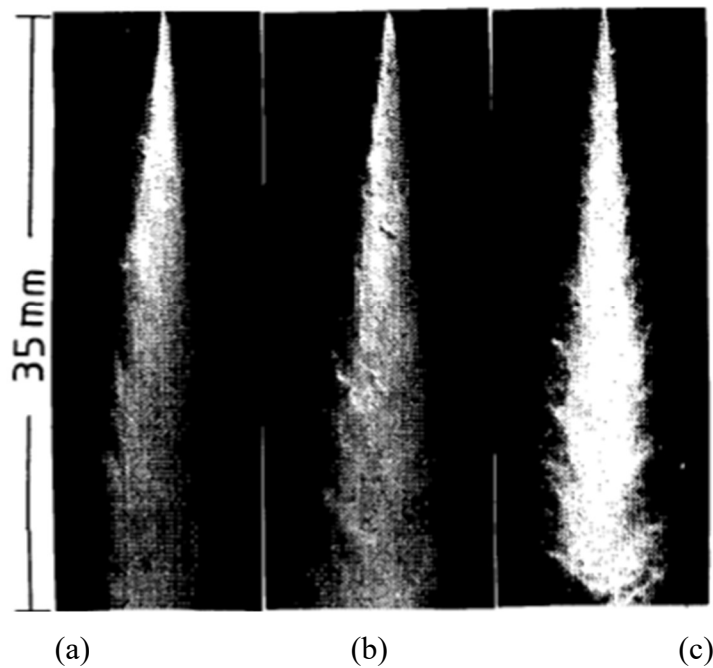
Figure 10. Comparison of spray imaging using (a) LIF (b) Mie scattering (c) Shadowgraphy [33]

When laser light is passed through a scattering medium, a small fraction of the incident photons comes out of the system without having undergone any collisions with the scattering medium. These coherent photons are called ballistic photons. Another form of shadowgraphy uses ultrashort optical-Kerr effect (order 2 ps) time gating to enhance the relative intensity of ballistic versus multiply scattered photons. Imaging using fast time gating helps to capture only the ballistic photons and the resulting image has a higher resolution due to prevention of the scattered light from smearing the image. Ballistic imaging has been used widely due to the significant enhancement in image contrast [50], [51]. Figure 11 shows the comparison between time-gated ballistic-photon imaging and conventional shadowgraphy. Techniques such as shadowgraphy and ballistic imaging are averaged along the line of sight. In this work, the focus is on tomography with Mie scattering, although it is also possible to employ tomography using techniques such as shadowgraphy and ballistic imaging to provide three-dimensional information.
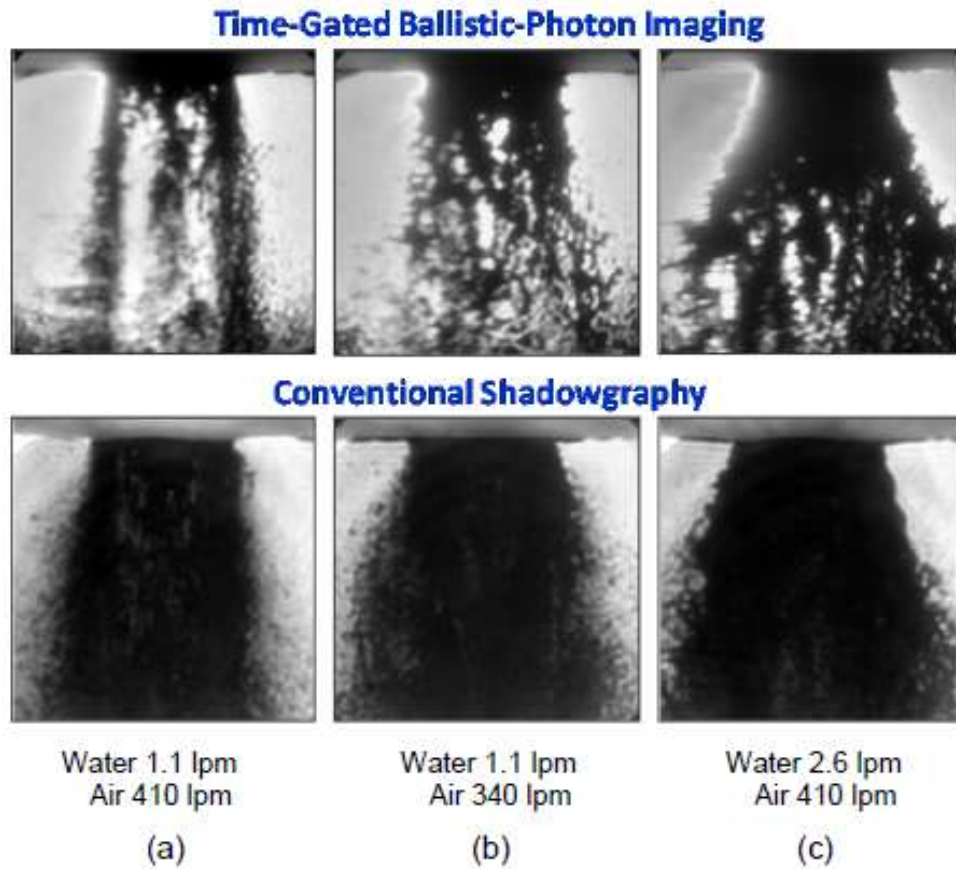
Figure 11. Comparison of ballistic images with shadowgraphy at different water and air flow rates for the same viewing area [10]

1.4 Three-dimensional Imaging Techniques

For complete understanding of the structures of multiphase flows, two-dimensional imaging is insufficient. As most features are three-dimensional, vital field data may sometimes be lost due to simply imaging in a single plane. Three-dimensional imaging helps to overcome this through the study of the intricate details of the structures throughout the imaging volume.

1.4.1 Plenoptic Imaging

In multi-lens-based plenoptic imaging, a recorded image is obtained using a multi-lens array in front of a camera, mimicking a situation wherein many individual cameras capture images of a target region from a large number of slightly different perspectives [9]. Figure 12 shows a sample setup for plenoptic imaging. The main tradeoff of using this method, however, is the reduction in image resolution due to multiple images being taken by a single camera. Plenoptic imaging has been used for spray imaging in the past [52]–[54].
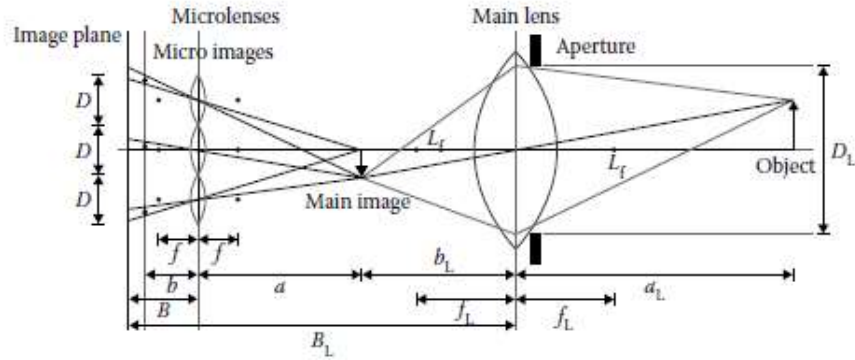
Figure 12. A sample configuration used for plenoptic imaging [9]

More recently, a modified version of the plenoptic imaging system, called the wide-angle relay plenoptic (WARP) imaging system has been developed by Halls *et al* [55]. The imaging system comprises a combination of four mirrors, each connected to a 90° prism held in a prism holder. The arrangement of prisms and mirrors is such that they focus on one top, one bottom, and two side views of the region under study (Figure 13). The four views are then sent into a single camera. The biggest advantage of this system is the ability to reduce the number of cameras by

four and still obtain wide angles to image three-dimensional fields more accurately. However, this method also suffers from the loss of resolution seen in the previous plenoptic setup. Despite this, the system holds a lot of promise for imaging of multiphase fields. Our group has been working on the application of this technique to blasts and combustion diagnostics [7], [55]. The current thesis also focuses on this method for target imaging.
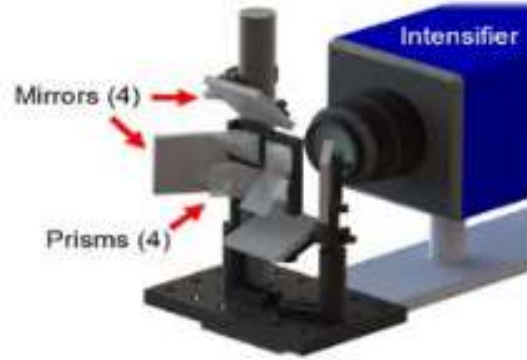
Figure 13. Quadscope developed for the purpose of WARP imaging [55]

1.4.2 Holography

Holography is a method in which a single-shot image of a sample volume illuminated by a coherent light beam is captured. The measurement volume is a cylinder with diameter equal to beam diameter and length equal to the depth of the object under study, for instance a spray. As the pulse duration is very short (~20 ns), the field may be considered frozen even if dynamic [9]. As the beam passes through the field, light is scattered off each droplet which then acts as a point source of diffracted light and results in interference patterns when mixed with the reference light beam on the holographic plate. Hence, a complete three-dimensional image of the field is obtained by this method. The captured image, called a hologram, can be used to recreate the original field by illuminating it with the same reference beam that was used to create the hologram. The light from the reference beam is scattered from the plate to reproduce the point sources representing each drop from the experiment [10]. The general setup for a holographic imaging system can be seen in Figure 14.

No calibration is required for the use of this technique in principle as the accuracy is set by the wavelength of light. Typically, droplets of ~15 μm can be resolved by this method. Holography

has been used by several researchers for spray diagnosis [56]–[58]. For very dilute (at least 80% transmission) sprays, rather than the split beam arrangement, a method called in-line holography is used, wherein the light scattered from the droplets is combined with the light transmitted through the spray [59], [60]. Sample results for a DIH experiment have been shown in Figure 15.
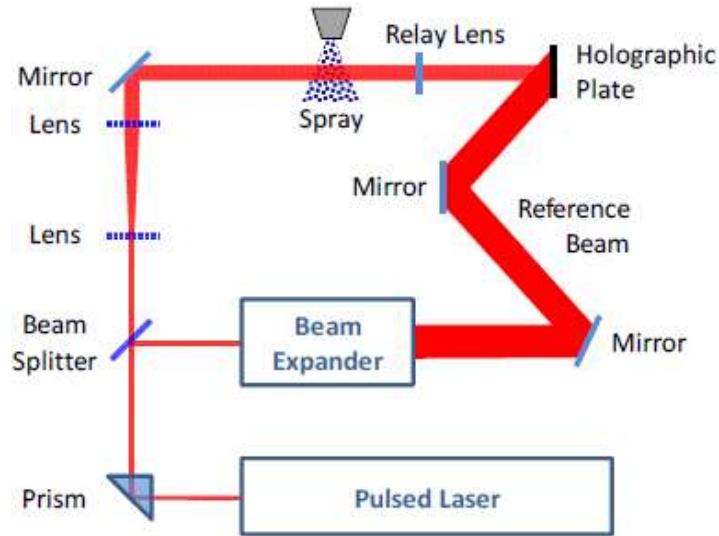
Figure 14. Basic setup for holographic imaging of a spray [10]
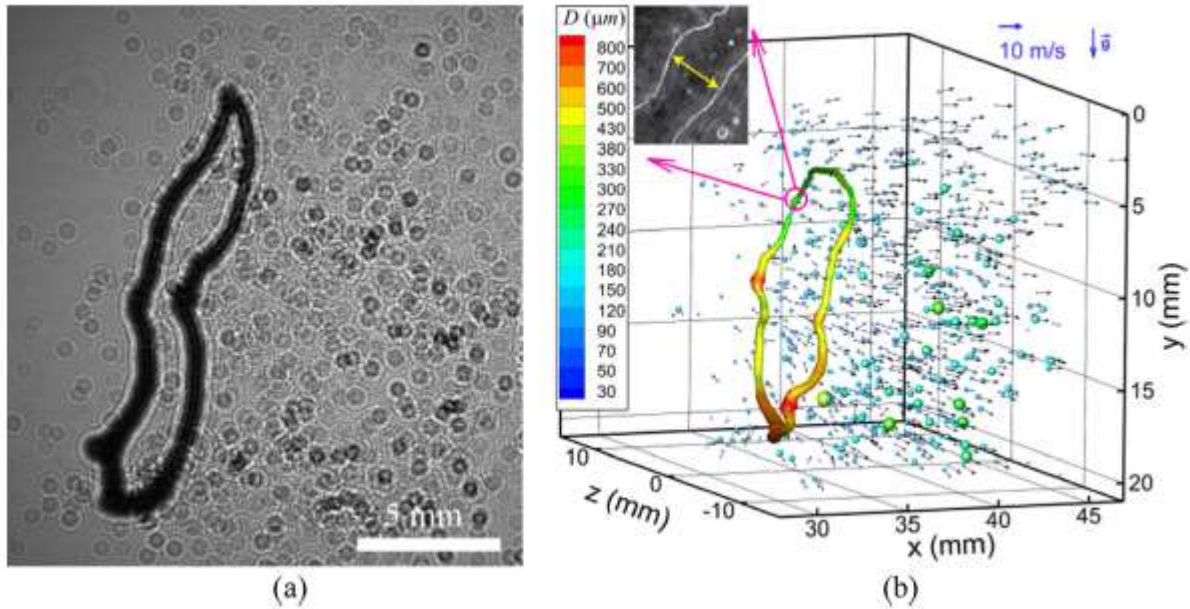
Figure 15. Example DIH results for the breakup of an ethanol drop in an air-stream (a) Experimental hologram; (b) Three-dimensional three-component particle field measured from this hologram pair [60]

28

The main disadvantage of DIH is that it can only be used for very dilute sprays. Some researchers have recently attempted the use of two view DIH for better visualization of dense sprays [61]. The setup for the same has been shown in Figure 16.
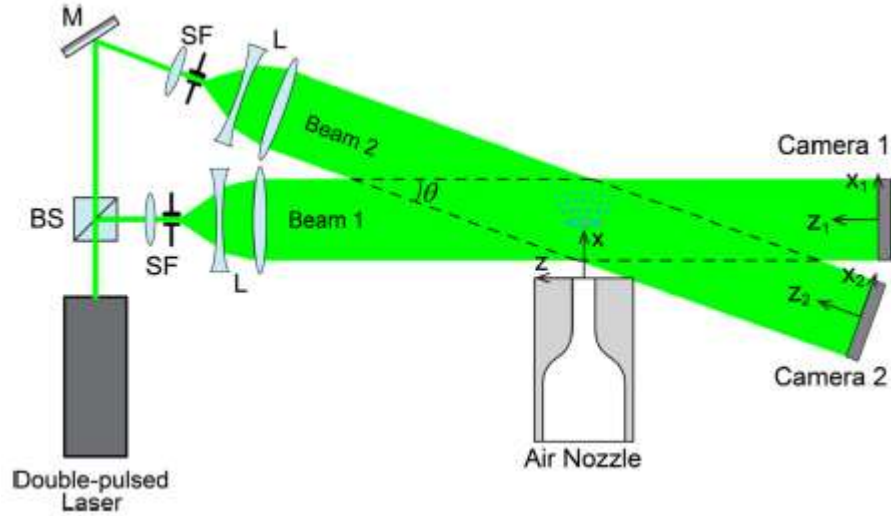
Figure 16. Setup for two-view DIH [61]

Despite its many advantages including the requirement of a single camera for 3D reconstruction in most cases, this approach is ultimately limited by shadowing along the line of sight. Due to the limitations of DIH in reconstructing complex flow structures and dense fields, it is of interest in this work to consider tomographic imaging along multiple lines of sight. It should also be feasible to extend DIH to multiple views, at the cost of significantly higher computational and processing time.

1.4.3   X-ray imaging

X-rays are a form of electromagnetic radiation that are produced by the ionization of a test target. They generally penetrate an object of interest in straight lines with minimal scattering, and their absorption depends on the material through which they pass. Owing to this nature, they are widely used in the imaging of dense multiphase fields [62]. For this purpose, a dopant is generally added to the field in a limited concentration to optimize the absorption rate of the field. X-ray imaging is mainly affected by the spatial, temporal, and density resolution of the system. X-rays

have been used in applications like studying fluidized beds, flows through casting hoppers, spray imaging, and cavitating flow studies among others. Several methods of X-ray imaging may be used. X-ray stereography uses information from 2D projections of the field to calculate the 3D features in the field. X-ray computed tomography, a process based on the mathematical reconstruction of a function based on multiple projections, is another widely used method for multiphase fields [63], [64]. Figure 17 shows the reconstructed images from X-ray computed tomographic studies, showing the liquid mass fraction iso-contours for the solid cone spray. Figure 18 shows a sample X-ray computed tomography image for the interior and horizontal sections of a flat spray as well as a hollow cone spray.
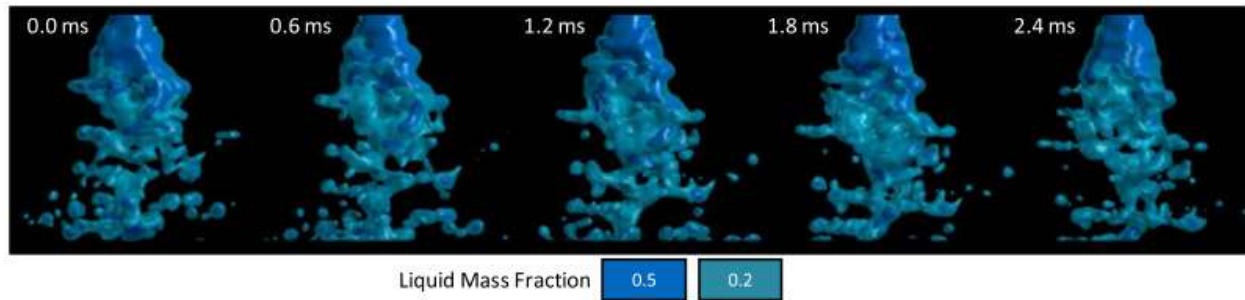
Figure 17. Time-evolving 3D isocontours of liquid mass fraction for a solid cone spray [63]

(a)   (b)
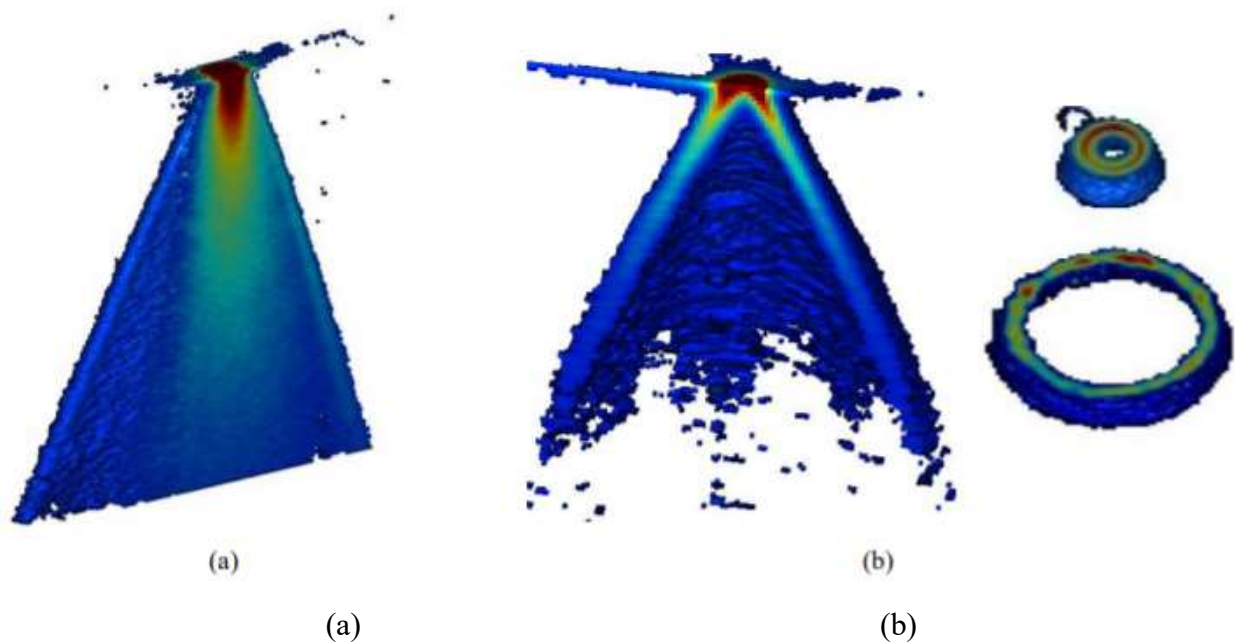
Figure 18. Sample X-ray computed tomography images for (a) flat spray; (b) the interior and horizontal sections of a hollow cone spray [64]

While this is a powerful technique for resolving three-dimensional multiphase fields, sustained high-speed imaging is limited by the photon flux of typical high-power X-ray sources. On the other hand, high power flash X-ray sources are limited to only a few sources, which can provide several snapshots at very high rates, but only few frames. As such, it is of interest to utilize optical tomography for sustained high-speed imaging of multiphase fields.

1.5   Tomographic Reconstruction

Tomography refers to the process of imaging a volume in the field by sectioning it using penetrating waves. Mathematic procedures are used to evaluate a complete representation of the volume through the application of various algorithms. The algorithm used may either be filtered back projection (FBP) or iterative reconstruction. In FBP, the image is directly calculated in a single reconstruction step, while in iterative reconstruction, reconstruction is like an inverse problem (studying causal factors from a set of observations). While both result in inexact results, FBP requires less time whereas iterative reconstructions leave less artifacts (reconstruction errors) after reconstruction [65]. The first development of tomography was by the radiologist Alessandro Vallebona in the 1930s. The method developed, called focal plane tomography, imaged a single plane at a time such that the focal plane appears sharp while all the other planes appear blurred. It was well into the 1970s before this method started getting replaced by computed tomography.

A typical 3D dataset is a group of 2D slices of the volume taken at regular intervals. Each volumetric element, called a voxel (pixel equivalent for volumes), is represented by a single value which is obtained by sampling the immediate area surrounding the voxel. For viewing the 3D reconstructed volume, iso-surfaces (a surface representing all points having the same value) are widely used. Figure 19 shows the basic model used for tomographic reconstruction.
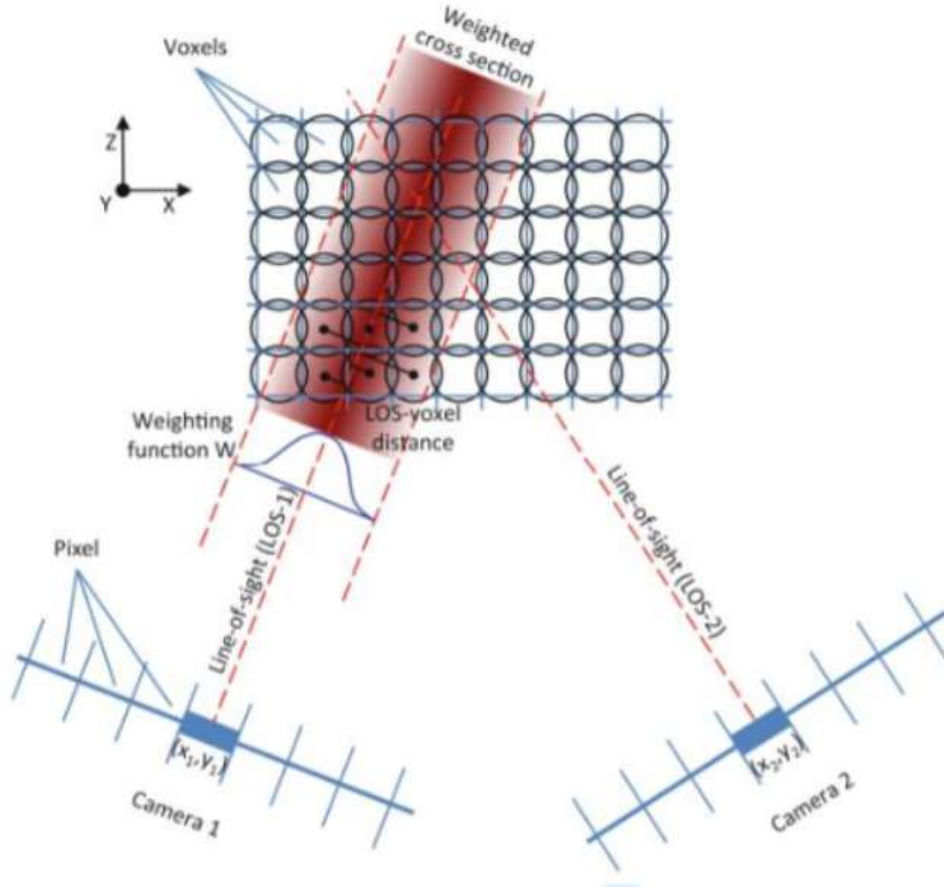
Figure 19. Representation of the reconstruction model for tomographic imaging [66]

Each iterative algorithm starts from an assumed image and updates the image based on the difference between the calculated and actual projections. Generally, inversion is based on the Radon transform, a method introduced by Johann Radon in 1917 [67]. The Radon transform is the integral transform that takes a function *f* defined on a plane to a function *Rf* defined on the 2D space of lines in the plane whose value at a particular line is equal to the line integral of the function over the line. The Radon transform represents the projection data obtained as the output of a tomographic scan and can be used to reconstruct the original field. The resulting image is called a sinogram. The term sinogram comes from the property of the Radon transform being a sinusoid for an off-center point source. Hence, the Radon transform tends to appear graphically as a number of blurred sine waves with different amplitudes and phases for a number of small objects. Lighter regions indicate areas of larger function values while black regions indicate zero value.

Algebraic reconstruction technique (ART) is an iterative reconstruction technique which reconstructs an image from a series of angular projections (a sinogram). It was first proposed by

Gordon, Bender, and Herman in 1970 [68]. The method involves starting from an initial guess and refining the solution using either the multiplicative method or the direct additive method. The total density of a plane (T) and initial guess for the density field (ρ_{ij}^0) is assumed to be,

$$T = \sum_{k=1}^{r_\theta} R_{k\theta} = \sum_{i=1}^{n} \sum_{j=1}^{n} \rho_{ij}$$

$$\rho_{ij}^0 = \frac{T}{n^2} \text{ where } i, j = 1, \dots, n$$

Considering $N_{k\theta}$ to be number of grid points for ray k of projection θ, the optical density of the same point at iteration q ($R_{k\theta}^q$) would be,

$$R_{k\theta}^q = \sum_{N_{k\theta} \text{ points } (i,j) \text{ in ray } (k,\theta)} \rho_{ij}^q \ \text{ for } k = 1, \dots, r_\theta$$

where ρ_{ij}^q is the qth approximation of ρ_{ij}. Two methods were proposed to refine this initial guess. The first method is the direct multiplicative method (MART). For this method,

$$\rho_{ij}^{q+1} = \left(\frac{R_{k\theta}}{R_{k\theta}^q}\right) \rho_{ij}^q$$

for (i, j) in ray (k, 0). The second method is the direct additive method. By this method,

$$\rho_{ij}^{q+1} = \max\left[\rho_{ij}^q + \frac{R_{k\theta} - R_{k\theta}^q}{N_{k\theta}}, 0\right]$$

These formulae were used for all rays for a given projection θ before moving on to the next projection. Converging to a stable solution seems essential for both methods.

Later studies comparing these as well as other algebraic reconstruction techniques have shown that the MART algorithm is the best approach for tomographic reconstruction of volumes [69]. For this reason, MART iterations were used in the current work for tomographic reconstruction.

1.6   Motivation

Three-dimensional imaging is essential to be able to visualize and inspect the multitude of structures and behaviors of multiphase systems. Majority of the prior work deals with imaging of particle fields, for instance finding the presence of a particular radical or soot particles in combustion systems [5], [6], [27], [70], [71]. However, it is also equally important for the imaging

of three-dimensional structures in the field which may not be estimated as particles like, for instance, sprays. Understanding many practical systems is linked to a good knowledge of the underlying characteristics. To be able to get good dimensional and structural information for the different stages of the spray as well as its typically non-uniform nature, it becomes important to get good two- and three-dimensional images of the same. While some researchers have worked on two-dimensional [20], [35] and three-dimensional [63] phase separation studies in the past, this domain still holds a lot of scope for research.

While accuracy of 3D fields has been performed before [3], [63], to the best of our knowledge, this is the first time that different targets and shapes are used for thorough evaluation of geometries and viewing angles of an imaging system.

1.7   Overview and Thesis Organization

This thesis focuses on the analysis of the accuracy and efficiency of a three-dimensional imaging system under development. The aim of the study is to use the imaging system to image three-dimensional structures with known geometries and post-process these images to quantitatively measure the accuracy of the designed system. Different orientations and number of views have been attempted and the goal is to design the best imaging system which would be used for further studies on multiphase fields.

Chapter 2 of this thesis focuses on the experimental setup used for the imaging studies and the methodology adopted for experimentation. Chapter 3 details the pre-processing methods used for the captured images and the procedure used for quantitative measurements. It also details the effect of varying multiple parameters on the reconstruction quality and the efficiency of the system in different target fields. Chapter 4 summarizes the major results and conclusions. Finally, Chapter 5 discusses the future scope of the work done as a part of this thesis.

2. METHODOLOGY

The aim of the study was to determine the best possible camera orientation, position, and number of views necessary to obtain the best reconstructions. To evaluate the accuracy with known geometries, 3D printed targets were imaged using two cameras in conjugation with a quadscope each. The targets were illuminated with the help of two LED lights. Details of each component used have been discussed below.

2.1   Experimental Setup

2.1.1   Quadscope

The quadscope is a device that is used to collect four different views for an object and transmit them to a single camera. A CAD model of the quadscope has been shown in Figure 20. A unique arrangement of four prisms and four mirrors with a broadband visible light reflection coating enables images of the top, bottom, right-hand side, and left-hand side of the object under study to be transmitted to a single camera. Each image occupies a separate quadrant of the camera pixels such that they can easily be separated later by splitting the image about the vertical and horizontal central axes. The quadscope mirrors may be adjusted to use viewing angles in the range of 10° to 50° and may be coupled to different cameras based on the requirement. Two such quadscopes have been used so that a total of 8 views are available for the object being studied. The angle between these two quadscopes has been varied as 90°, 135°, and 180°. The distance between the quadscope and the target has also been maintained at either 4 inches or 7.5 inches for all experiments. The quadscopes are adjusted so that the path lengths of all the images are the same and all the quadrants for the camera focus at the same point. The quadscope was built such that for each prism-mirror combination, the distance between the mirror and prism is 1 inch. The angular separation between the two is set to about 30° in each case.
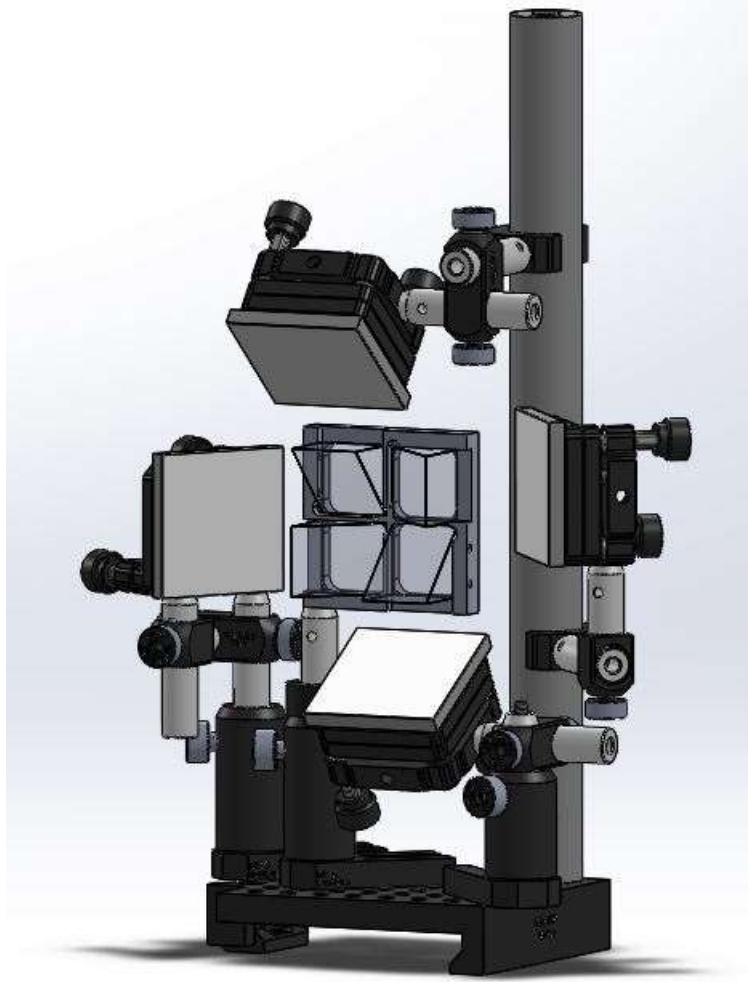
Figure 20. CAD model of the quadscope used for experiments

2.1.2 Camera

Two highspeed Phantom V2012 CMOS cameras (Figure 21) by Vision Research were used for capturing images. The cameras were coupled with 50 mm f/1.4 lenses for all setups with an additional 8 mm extension ring attached to the camera to enable visualization at only 4 inches away. The Phantom V2012 has a maximum resolution of 1280×800 and has a sensor with a 28 μm pixel size. The maximum resolution was used to obtain the best images. The camera had a scale factor between 10 and 11 pixels/mm for the different orientations as verified by LaVision's DaVis 10 software in which the images were processed. The calibrated images were obtained within a maximum of 0.2-pixel to 0.5-pixel error, which corresponds to an uncertainty of about 0.005 to 0.014 mm. The quadscope position is adjusted so that it splits the image exactly along the

vertical and horizontal central axes of the camera capture, as confirmed using the Phantom Camera Control (PCC) software. Each quadrant is ensured to have a centered image, one from each quadscope prism-mirror pair. Figure 22 shows one such centering wherein the LaVision 058-5 3D calibration plate is used.

Figure 21. The Phantom V2012 camera by Vision Research
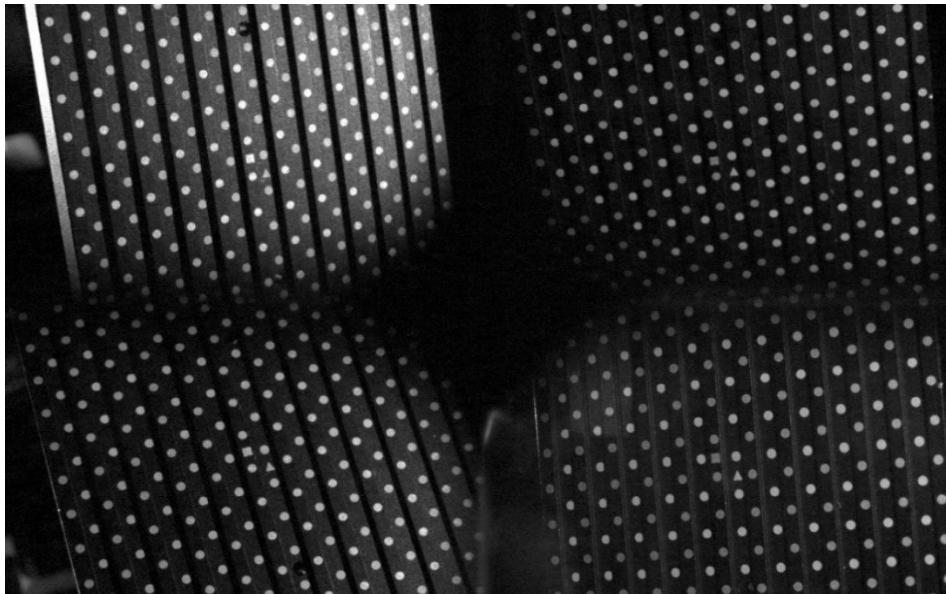
Figure 22. Image captured by a camera during centering with the LaVision 058-5 3D calibration plate

2.1.3 Illumination Source

For even lighting, two ThorLabs 800 mW mounted LEDs (MCWHL5) (Figure 23) were used. Each LED outputs cold white light with a correlated color temperature of 6500 K and more than 800 mW power. It is mounted to the end of a ϕ30.5 mm heat sink. The two LEDs were placed facing the targets from opposite sides. It was ensured that both cameras captured well-illuminated objects, while no direct light entered either camera from the LEDs for any of the 8 views.

Figure 23. Thorlabs MCWHL5 mounted LED

2.1.4 3D Printed Targets

CAD models of several varied geometries were developed in SolidWorks with the aim to study the effect of the number of views and the angle between the two quadscopes on different geometries. Some of these models have been shown in Figure 24. The targets are held in a conical base with a square recess at the top. Each target has a corresponding protrusion at the bottom which enable it to be inserted into the base with high repeatability. This ensures that all the models are placed exactly at the desired height and position, which was designed to be the same as that of the center of the dot target. Different geometries were developed such that they would represent different field characteristics like transparent droplets or shadowing due to solid particles.

38
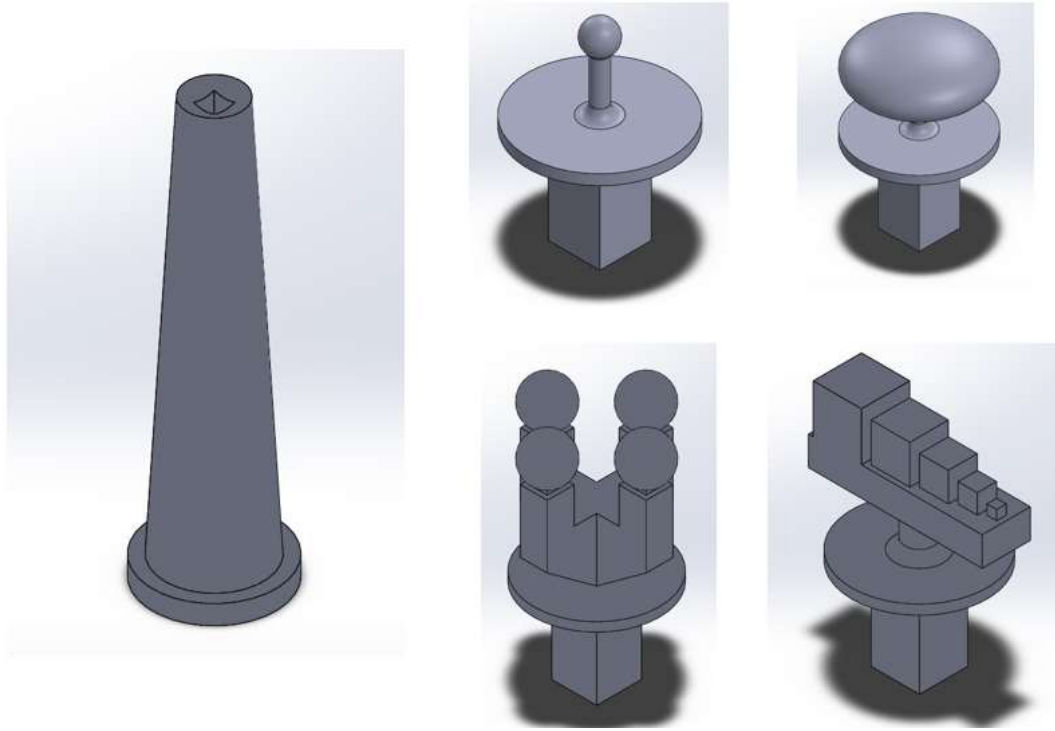
Figure 24. CAD models created for testing

The models were 3D printed in two different materials. The clear resin models (white) helped emulate flow conditions involving semi-transparent objects while the opaque flexible resin models (grey) helped to emulate solid bodies in the flow. Images captured for each of these materials have been shown in Figure 25. The effect of shadowing is clearly visible for the opaque object.

(a)   (b)
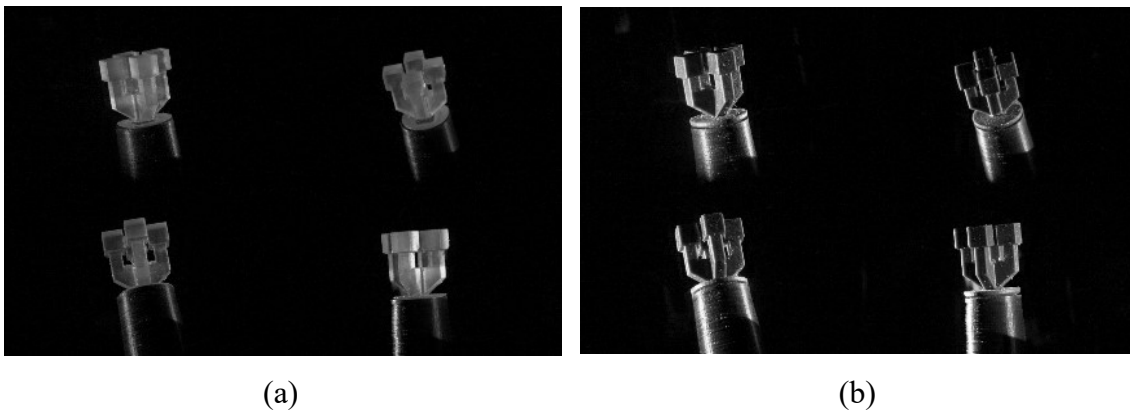
Figure 25. Images captured for the same model in the (a) clear resin and (b) flexible resin materials

2.2   Experimental Procedure

A set of eight mirrors and eight prisms were used to build two quadscopes with a focal distance equal to the separation distance. Back lighting was provided to the quadscope through the prisms using the MCWHL5 LED to ensure that all the four views were focused at the same location. This was ensured by placing a sheet of paper in the beam path at exactly at the desired separation distance from the quadscope and focusing the four squares resulting from the backlighting of the prisms at the exact same location at the axis of the quadscope, recreating the image of the prism holder. The mirrors were adjusted so that the distance of each mirror from its corresponding prism was equal to 1 inch. The mirrors were rotated about the x and y axis with the help of two knobs until all the back-reflected images showed the same identical overlapping squares. This ensured that the path lengths for all the images were identical and that all the images were focused at the same region in space.

The quadscopes were arranged on optical rails at equal separation distances from a LaVision 058-5 3D calibration plate. The separation distance was varied at 4 inches and 7.5 inches. For the 180° and 135° camera arrangements, the camera-quadscope pair were arranged such that they viewed opposite sides of the calibration plate. Meanwhile, for the 90° arrangement, both the cameras were arranged such that they focus on the same face of the calibration plate. The cameras were set up behind the quadscope such that it was centered with respect to the quadscope, as ensured from the images captured with the help of the PCC software. The vertical and horizontal splitters on the quadscope prism holder which separate the four prisms were centered about the horizontal and vertical axes of the camera. The focusing and centering of the system was confirmed by trying to image the same point on the target through all the eight views. The location of the central point was confirmed to be the same for each image.

The calibration target was imaged at about 10 to 15 orientations at different axial locations within the depth of view as well as angular rotations about different axes. The captured calibration images were loaded into the tomographic reconstruction module of the DaVis 10 software by LaVision (a commercial image processing code) to calibrate the eight camera views. The pin-hole model, in which all the light is assumed to pass through a single point, is used to obtain the necessary software calibration. The calibration target is now replaced by the 3D printed targets placed on the holder. The holder has been designed such that the object, after placing it on the holder is at the same height as the center of the calibration target. This ensures that the calibration

and imaging are done at the same location. These captured images are then imported into DaVis 10 for further processing.

Figure 26 shows the complete experimental setup that was used for the both the 180° and the 90° camera orientations. The image captured for one of the targets used is visible in the 90° arrangement.
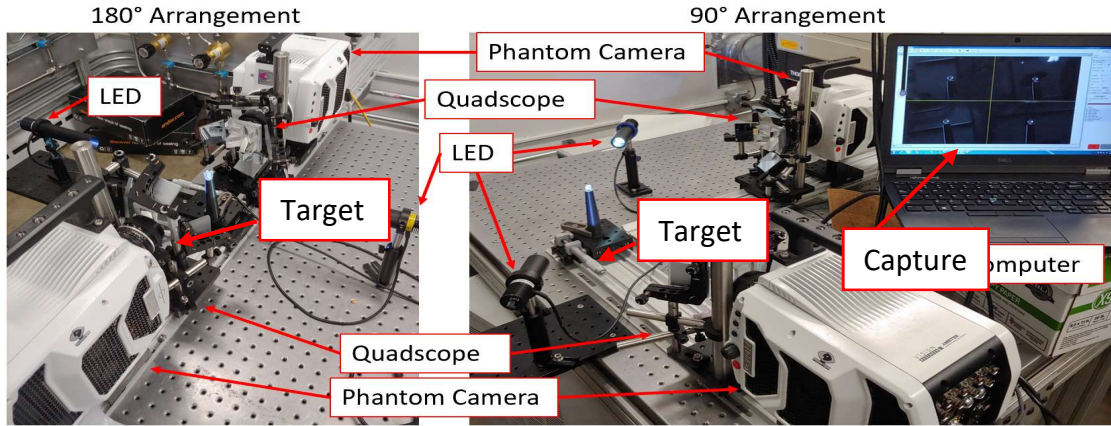
Figure 26. Experimental setup showing two different orientations for the quadscope-camera pairs highlighting all major components used

The images were captured in a dark room illuminated only with two MCWHL5 LEDs. This helped to cut out considerable background noise. However, some artifacts remained in the images. In order to clear these, the captured images were pre-processed before performing tomographic reconstructions by the application of various filters. Table 1 shows the effective camera angles obtained around the object.

The imaged volume was reconstructed with the help of a multiplicative algebraic reconstruction technique (MART) algorithm in the LaVision DaVis 10 tomographic software. The iterative algorithm uses the data from the captured images to estimate a volumetric field from a set of linear equations. The algorithm then corrects the volume until there is no change in the projections of the volume. The resulting reconstructed volume is a 3D intensity map of the measured flow field. Smoothening was performed after each MART iteration. The reconstruction was limited to the localized region where the object was centered, as ensured by trial test processing involving 5 MART iterations. This ensured that the processing time was minimized as larger reconstruction volumes require larger computation times. The main target of interest for

quantitative analysis was a sphere as shown in Figure 27. For the purpose of good comparison, a mask was applied before binarization such that only the spherical portion of the target was remaining at the end of the pre-processing. The result of this processing has been shown in Figure 27 part (b).

Table 1. Angular orientation of each view

ORIENTATION	EFFECTIVE CAMERA ORIENTATIONS (VERTICAL AXIS)	EFFECTIVE CAMERA ORIENTATIONS (HORIZONTAL AXIS)
90° ARRANGEMENT	-30°, 0°, 30°, 60°, 90°, 120°	-30°, 0°, 30°
135° ARRANGEMENT	-30°, 0°, 30°, 105°, 135°, 165°	-30°, 0°, 30°
180° ARRANGEMENT	-30°, 0°, 30°, 150°, 180°, 210	-30°, 0°, 30°
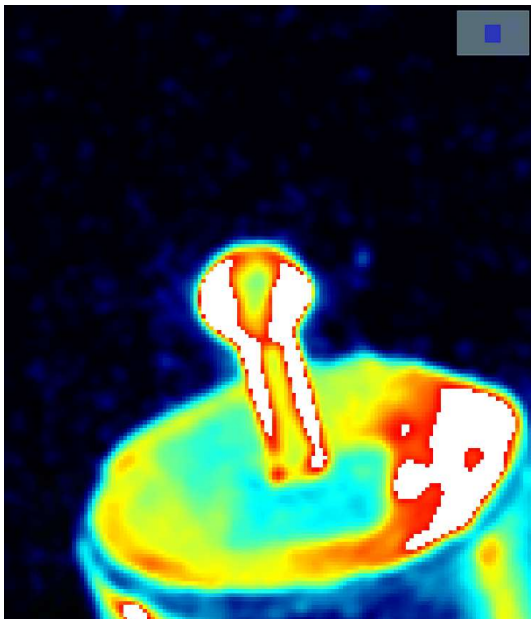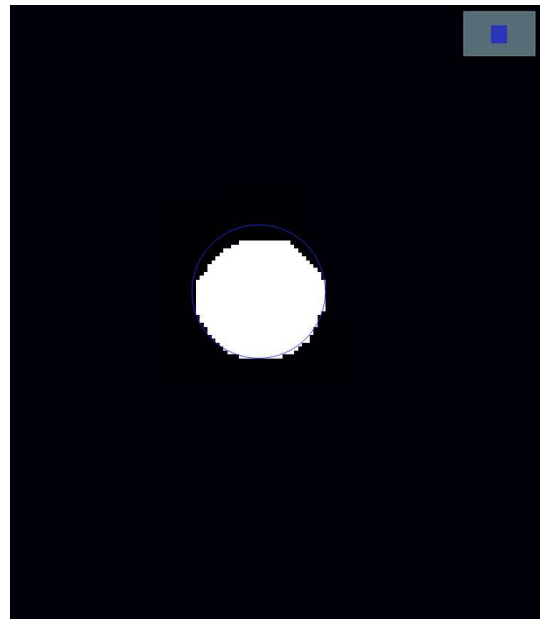
(a)   (b)

Figure 27. Effect of masking on the pre-processed image (a) Image before masking (b) Image after masking followed by binarization (mask applied can be seen in blue)

A MATLAB code was developed to find the diameter of the reconstructed sphere. The vertical, horizontal and two diagonal diameters were measured in each case in the XY, YZ, and XZ planes. A certain percent of the maximum intensity was considered as the boundary of the image for the same. The results for different number of iterations and camera views and orientations were compared to find the best possible combination such that the measured error is minimized.

3. RESULTS AND DISCUSSION

3.1 Data Processing Methods

3.1.1 Reconstructions Using DaVis 10

The raw images captured by the cameras are first pre-processed using the DaVis 10 software. As a quadscope is used in front of each camera to capture the images, four images are captured within a single frame. The two raw images are first split about the vertical axis followed by the horizontal axis. The resultant eight images are then combined to get a single set of eight frames and are further used for the reconstruction.

To ensure good reconstructions, it is essential to remove as much background data and noise from the images as possible. For this, after forming the dataset with all eight images, a median filter was applied. The median filter is a non-linear filter that replaces the value of each pixel with that of the median of the neighboring pixels. Significant noise reduction was possible through this method. Reduction in the noise and its intensity is also seen with the use of a Gaussian filter. A Gaussian filter is a linear filter which applies a Gaussian fit to an array of pixels around every pixel in the original image. However, some blurring of edges is also seen with the use of a Gaussian filter. Removal of smearing from the image also helps reduce noise and smearing caused by gaussian smoothening. It was observed that by applying the median filter, followed by the Gaussian filter, and finally, removal of smearing gave the best reduction of noise from the images. After this, the intensity of the noise is seen to be much lower than that of the object of interest.

To eliminate any remaining noise, binarization of the image is done such that a clean image is available for reconstruction. Binarization also helps to remove any inherent non-uniformities in lighting. The effect of using these filters individually as well as the application of the best combination of these filters (Part (e)), and finally binarization of the captured images has been shown in Figure 28.

The pre-processed images are reconstructed using the inbuilt MART algorithm in DaVis 10. Trials were conducted at iterations ranging from 5 to a 1000 for different experimental setups. Each iteration was followed by a smoothing iteration with a smooth strength of 0.5. The sparseness threshold was maintained at 0.

(a)   (b)

(c)   (d)

(e)   (f)
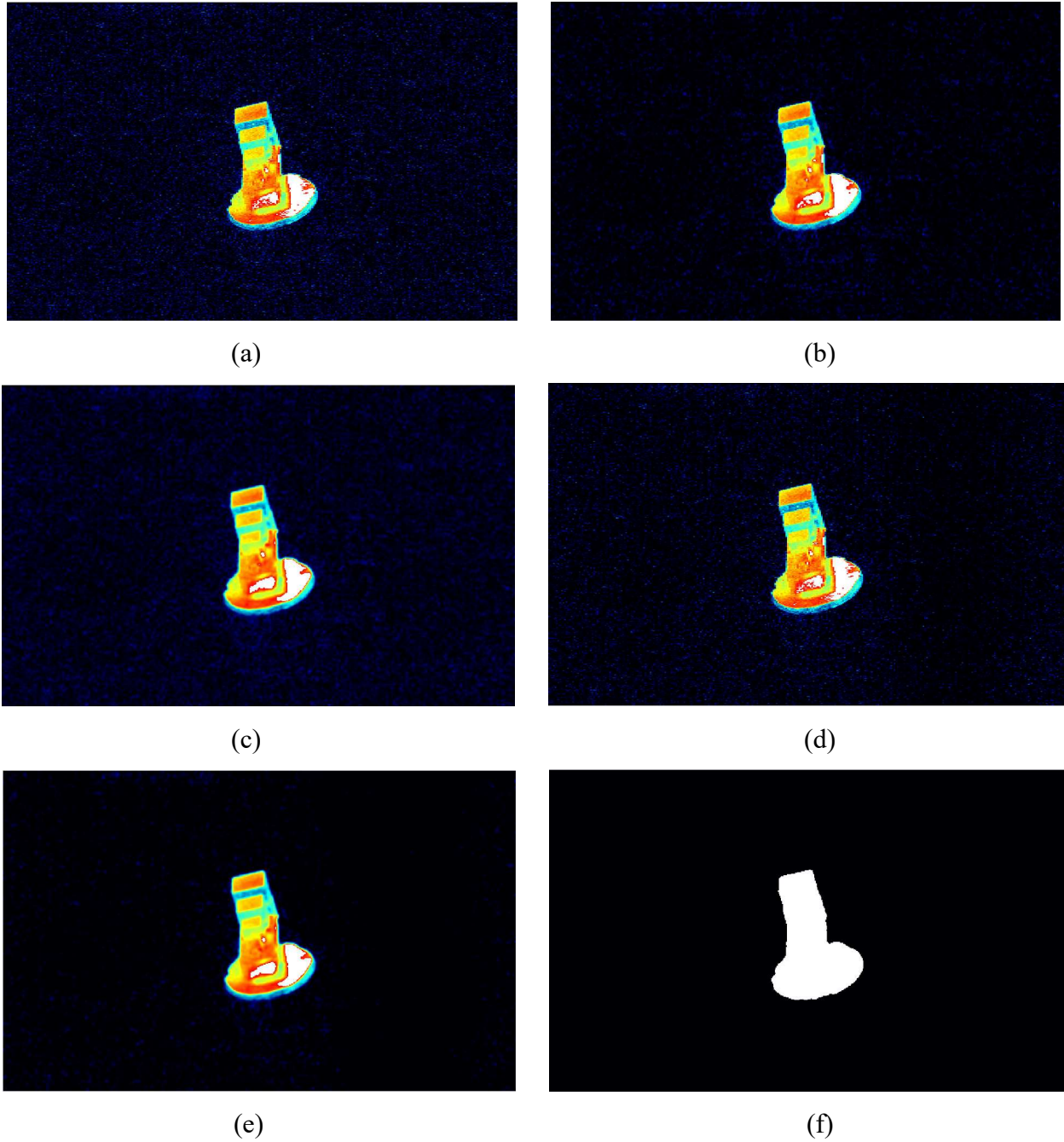
Figure 28. Effect of pre-processing on the captured images (a) Original captured image; (b) Median filter; (c) Gaussian filter; (d) Removing smearing; (e) Median filter + Gaussian filter + Removing smearing; (f) Final binarized image

3.1.2   Image Processing Using MATLAB

For the purpose of quantitative analysis, a MATLAB code was developed to measure the diameter of a reconstructed sphere. Masking is used for the captured images such that only the

45

spherical head of the target object is reconstructed. The reconstructed sphere is imported into MATLAB with the help of the *readimx* package by LaVision. The different planar slices obtained are put together to form a 3D matrix and the reconstructed volume is recreated with the help of a custom-designed code. The reconstruction is available in the form of an intensity distribution at each voxel (volumetric pixel) location. The highest intensity in the image is found and the boundary of the object is set by binarizing the image at a certain percent of that intensity. It was observed that the boundary could be set at a higher level for lower MART iterations, but the application of smoothing necessitated lower levels for higher MART iterations (Figure 29).

(1a)   (1b)   (1c)

(2a)   (2b)   (2c)
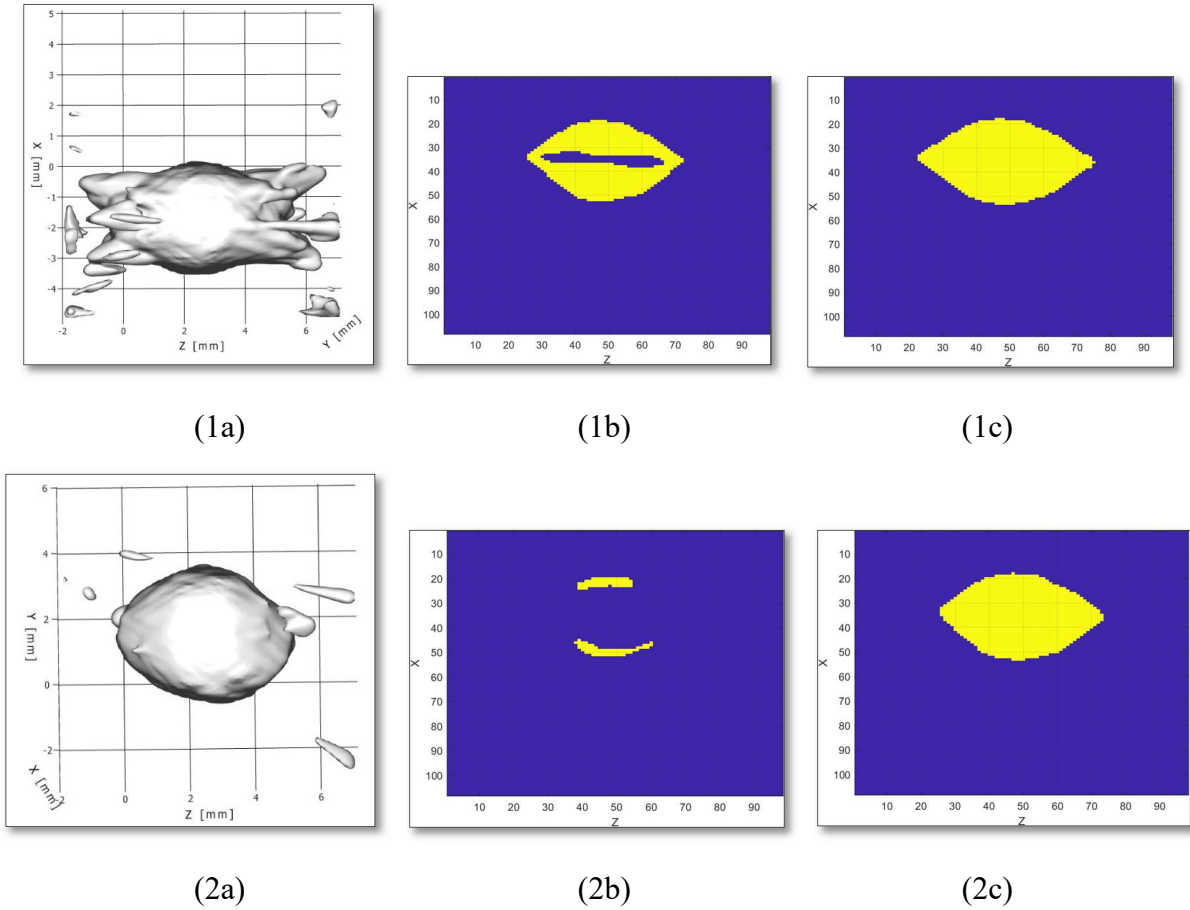
Figure 29. (1) 5 MART iterations vs (2) 1000 MART iterations for one of the processed images. (a) Actual side view of reconstructed image from DaVis; (b) Binarization at 28% of maximum intensity; (c) Binarization at 9% of maximum intensity

It was observed that different orientations have different levels of maximum intensity that can be utilized to get a completed image. In order to get a uniform threshold for comparing data,

all computations for measuring the diameter of the sphere were performed at 1% of maximum intensity. Analysis for the 4-inch separation distance was also performed at 5% of maximum intensity.

The midplane of each view (front, side, and top) was selected as that with the largest diameter. For each of these, the horizontal, vertical, and two diagonal diameters were measured. The measurement error was computed with respect to the converged solution (considered as the solution after 1000 iterations) as well as the true solution (design diameter of the sphere). For each plane, the root mean square of the four measured diametric errors is taken to find the root mean square converged solution error, rms_c, and the root mean square actual solution error, rms_a, for each plane. Finally, the root mean square of each plane's rms_a value is used to find the final error, rms_f, for each trial.

3.2 Data Analysis

3.2.1 Number of MART Iterations

It is hypothesized that with an increase in the number of MART iterations, the reconstruction quality should also improve, and the value of rms_a and rms_f would decrease.

The number of MART iterations were varied in steps from 5 iterations to 1000 iterations (maximum possible limit on DaVis 10). The camera orientations at 90°, 180°, and 135° were each compared at a distance of 4 inches and 7.5 inches between the quadscope and object under study. For each case, the image of a 3 mm sphere was reconstructed, and the measured diameter was determined with the help of the code. For every instance, it was observed that with an increase in number of iterations, the artifacts in the image decreases (Figure 30), and the rms_f decreases, until it finally stabilizes to a converged solution (Figure 31). Table 2 shows the number of iterations necessary for solution convergence for the different camera orientations.
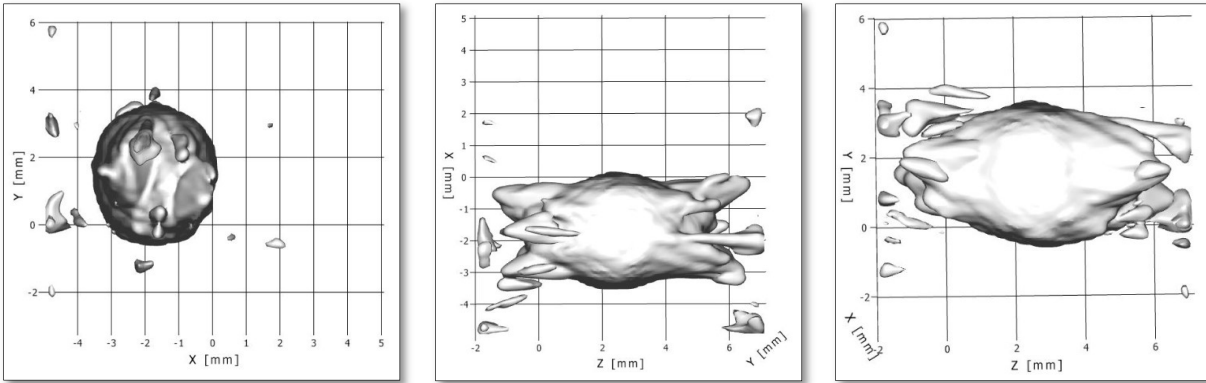
(a)
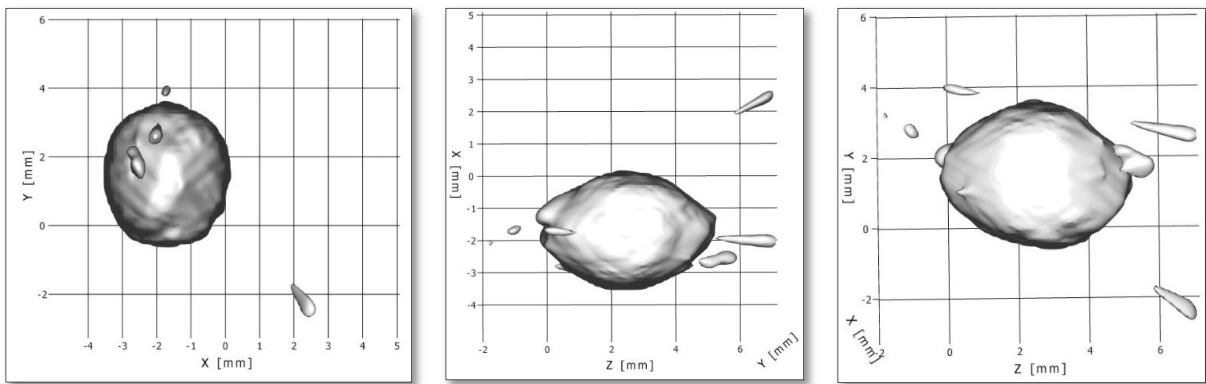
(b)

Figure 30. 135° camera orientation at a distance of 4 inches between quadscope and target showing reconstructions after (a) 5 and (b) 1000 MART iterations
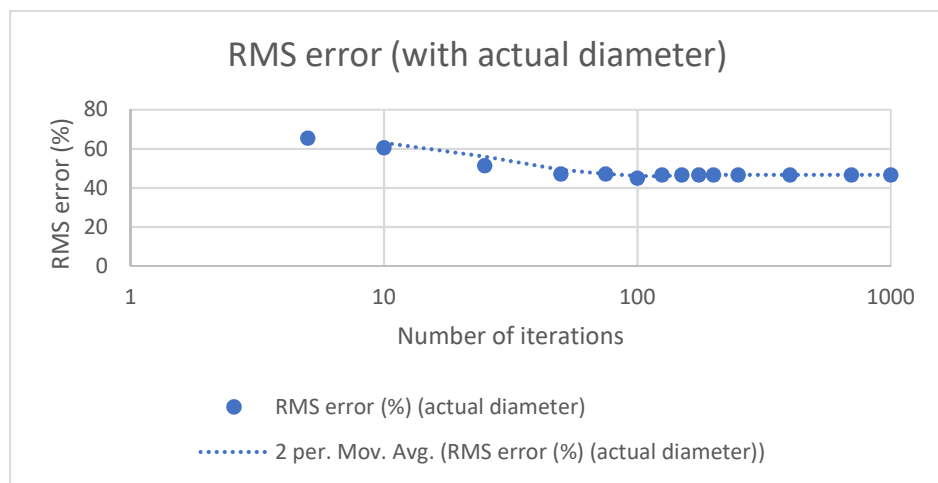
Figure 31. RMS error for 180° orientation of cameras for the YZ plane at a distance of 4 inches between the quadscope and target as a function of number of MART iterations with boundary at 5% maximum intensity

Table 2. Number of iterations needed for solution convergence for different test orientations with boundary at 1% maximum intensity

ORIENTATION	4 INCHES	7.5 INCHES
90° ARRANGEMENT	10	25
135° ARRANGEMENT	10	25
180° ARRANGEMENT	75	125

3.2.2   Camera Orientation

The angle between the two cameras was set at 180°, 135°, and 90° to study the effect of camera orientation on reconstruction quality. It is hypothesized that the depth information would be best for the 90° orientation as compared to the 135° (intermediate) or 180° (expected to be the worst).

For the 180° orientation, it was observed that the reconstructed images were highly stretched out due to the almost complete absence of depth information. The 180° orientation was also the easiest to calibrate with the two-sided 058-5 3D calibration plate. The reconstruction also suffered from large dimensional errors in the z-direction due to the depth information not being capture well. It was also seen that the most MART iterations were needed for convergence of the solution in this case. While good reconstructions of complicated geometry are possible in the camera viewing direction, the extreme loss of depth information poses a real challenge in identifying the internal structures.

At 135°, the reconstructions are seen to undergo some stretching but not as much as the 180° orientation. Internal structures are also easier to distinguish even though they are slightly skewed. The calibration is also easy for this case. Error is seen to be lower than the 180° orientation due to the improved depth information.

The images at 90° were difficult to calibrate due to limitations of the calibration plate being used. This resulted in only 6 images being used for calibration. Despite this, least iterations are required for convergence of the solution. The solution was also closest to the true solution for

closer orientations. The internal features are difficult to reconstruct due to the absence of wide-angle views. Similarly, at larger separation distances, this affected the reconstruction at 90°.

Figure 32 shows the different reconstructions obtained for a 3 mm diameter sphere at the different orientations. The projected views of all the directions have been included here. Figure 33 shows the percentage error computed for the YZ plane using the MATLAB code for all three orientations. The increase in error in the converged solution with increase in the angular separation is clearly visible.

| (1a) | (1b) | (1c) |

| (2a) | (2b) | (2c) |

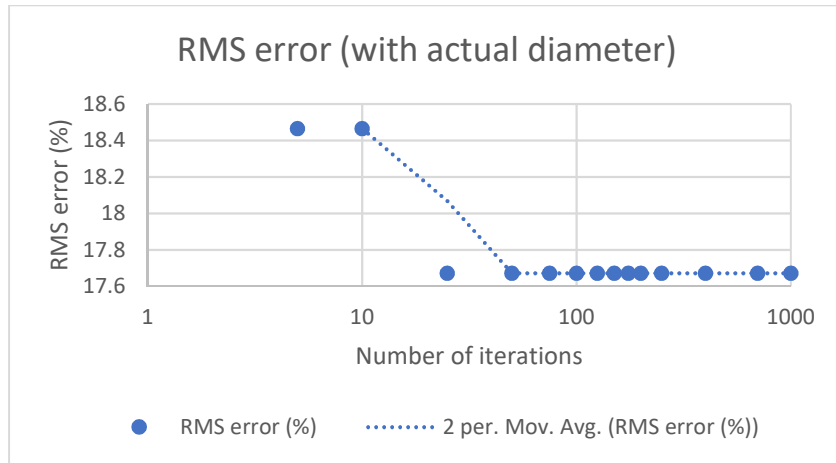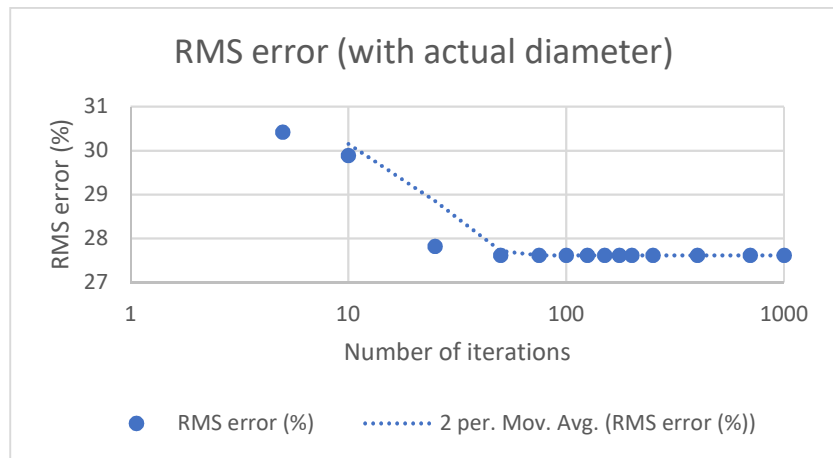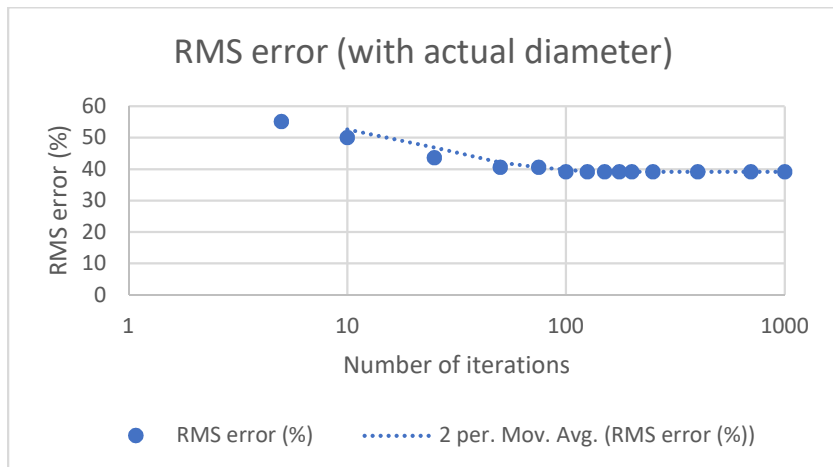| (3a) | (3b) | (3c) |
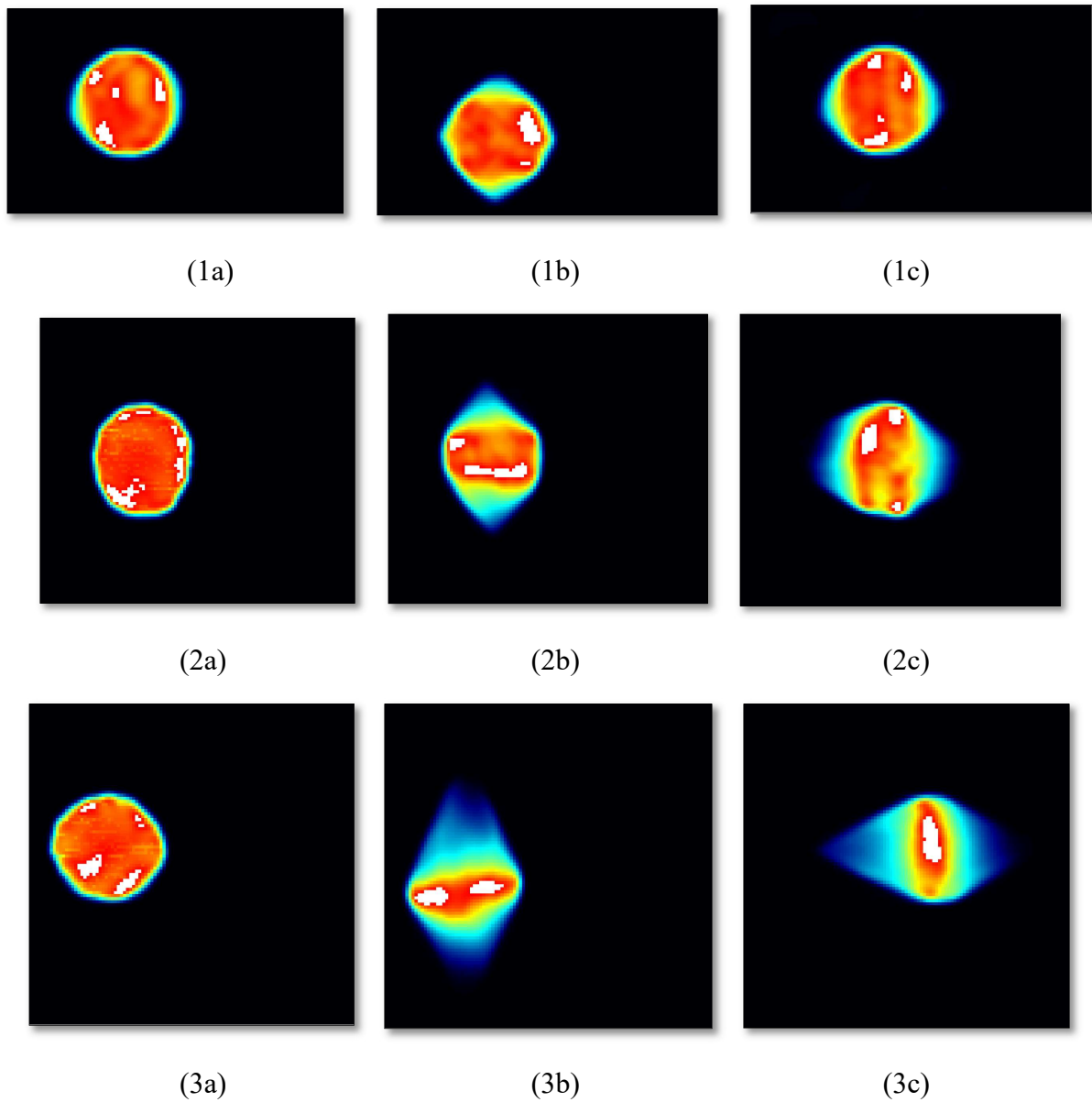
Figure 32. (1) 90°, (2) 135°, and (3) 180° orientation (4 inches) in (a) XY, (b) XZ, and (c) YZ planes

(a)

(b)

(c)

Figure 33. Absolute error in reconstruction for different camera orientations at 4 inches separation distance (a) 90°; (b) 135°; (c) 180°; for the 3 mm sphere considering boundary at 5% of maximum intensity

3.2.3 Distance Between Object and Imaging System

Measurements were made by maintaining the distance between the quadscope and the target at 4 inches as well as 7.5 inches. The hypothesis is that bringing the imaging system closer would increase the resolution of the images and hence reduce the error.

It was observed that the error for the 90° arrangement decreased on decreasing the distance from 7.5 inches to 4 inches while this effect was reduced considerably for 135° and almost negligible for 180°. Hence, it seems as if the effect of distance is also dependent on the angular separation between the two quadscopes. For the 90° arrangement, visible improvement in reconstruction quality is also seen, especially for internal structures. Table 3 shows a comparison for the percentage error at different quadscope orientations.

Table 3. Comparison of error (%) for different orientations and separation distances for the 3mm diameter spherical target with boundary at 1% of maximum intensity

ORIENTATION	4 INCHES SEPARATION DISTANCE	7.5 INCHES SEPARATION DISTANCE
90° ARRANGEMENT	22.5 %	47.1 %
135° ARRANGEMENT	32.9 %	43.7 %
180° ARRANGEMENT	51.9 %	56.0 %

It was also observed that the interior structures are reconstructed better when the separation distance is 4 inches rather than 7.5 inches. Figure 34 shows the projected views for the reconstruction of a combination of spheres at 135° for both 7.5 inches as well as 4 inches. Figure 35 shows the same for a combination of cubes at 90° angular orientation. The problems due to absence of two side views in the 90° orientation, are clearly visible. The reconstruction at 4 inches seems better than that at 7.5 inches. However, a separation distance lower than 4 inches should help to further improve the reconstruction quality.
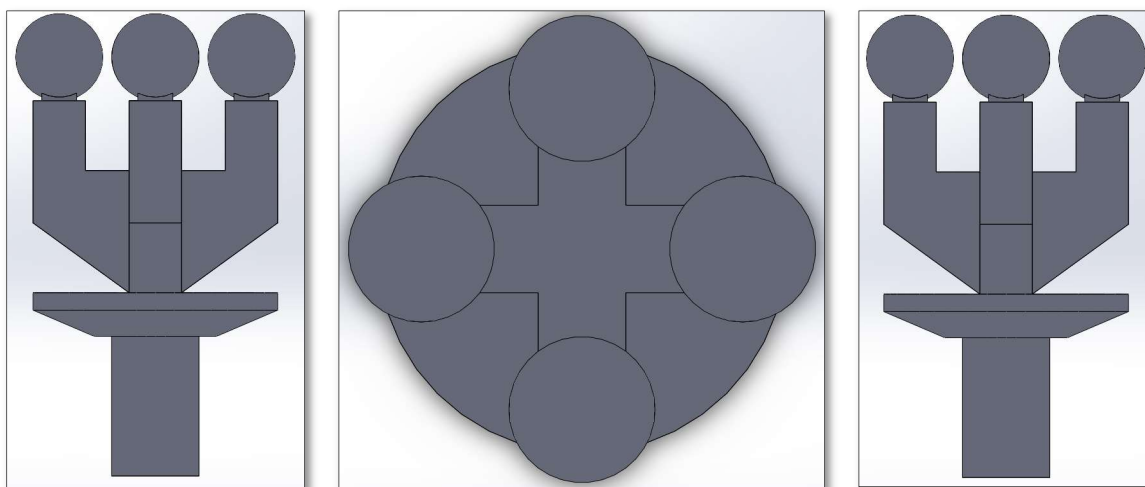
(a)
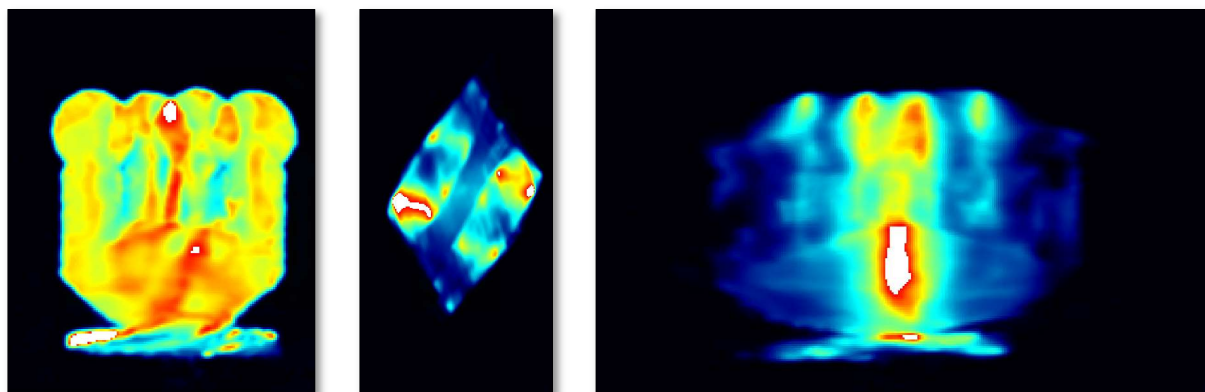
(b)
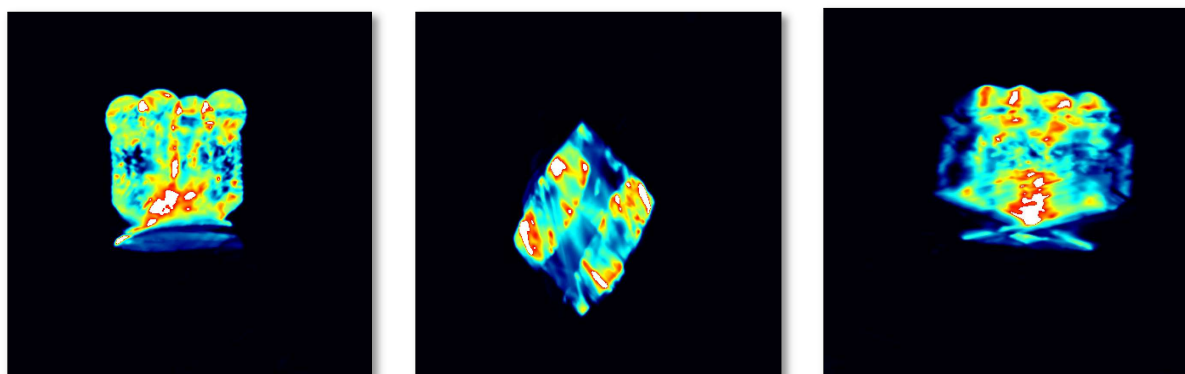
(c)

Figure 34. Projections of the reconstruction of a combination of spheres (a) CAD model designed; (b) 135° 7.5 inches orientation; (c) 135° 4 inches orientation
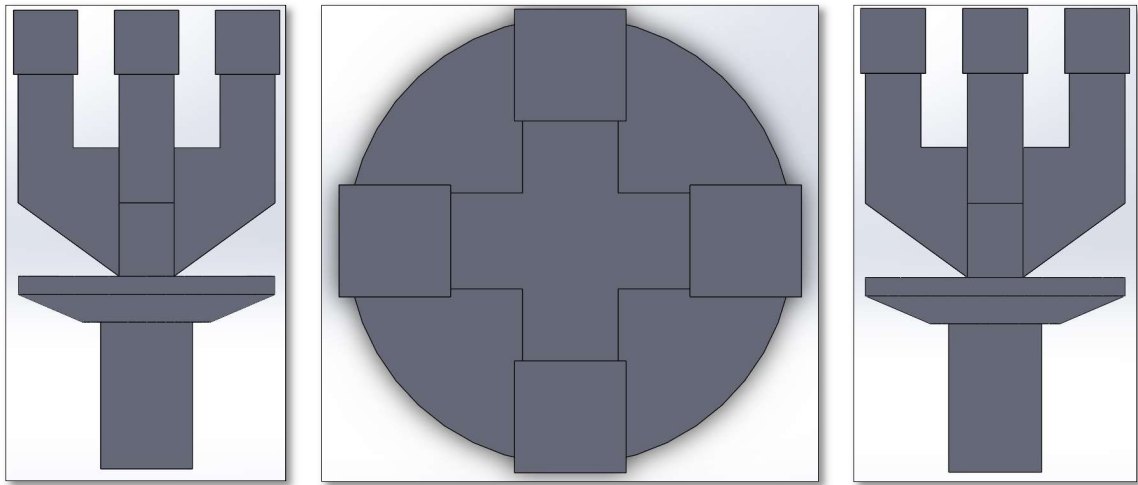
(a)
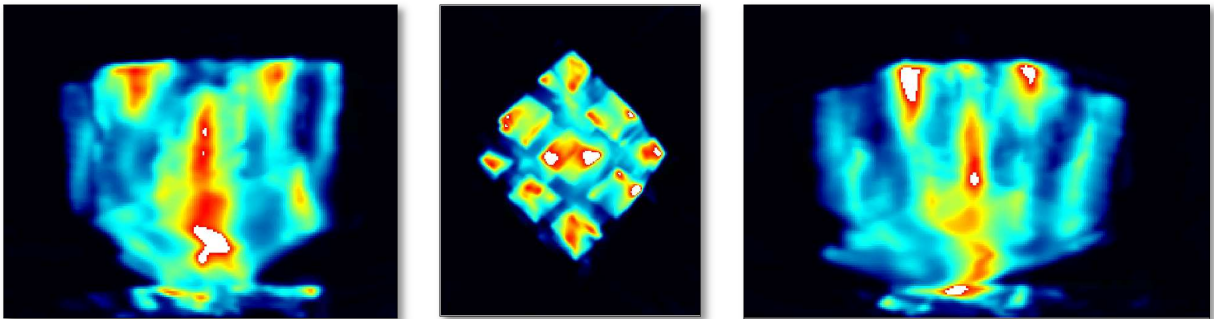
(b)
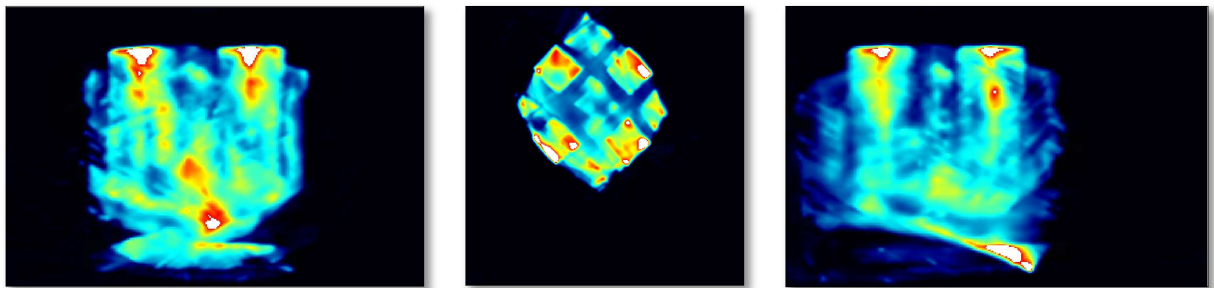
(c)

Figure 35. Projections of the reconstruction of a combination of cubes (a) CAD model designed; (b) 90° 7.5 inches orientation; (c) 90° 4 inches orientation

3.2.4 Object Size

The sphere reconstruction involved the use of 10 mm diameter spheres as well as 3 mm diameter spheres. It is hypothesized that larger objects would be more sensitive to angular separation than smaller objects due to the ability to image around the object better.

It was observed that while the smaller sphere converged to a solution after about 75 MART iterations, the larger sphere required about 700 MART iterations for the same. Hence, size of the object has a considerable effect on its speed of convergence. It was also observed that for opaque objects, smaller objects seem to be better illuminated and hence retains much more information than larger objects, as seen in Figure 36.

(a)

(b)
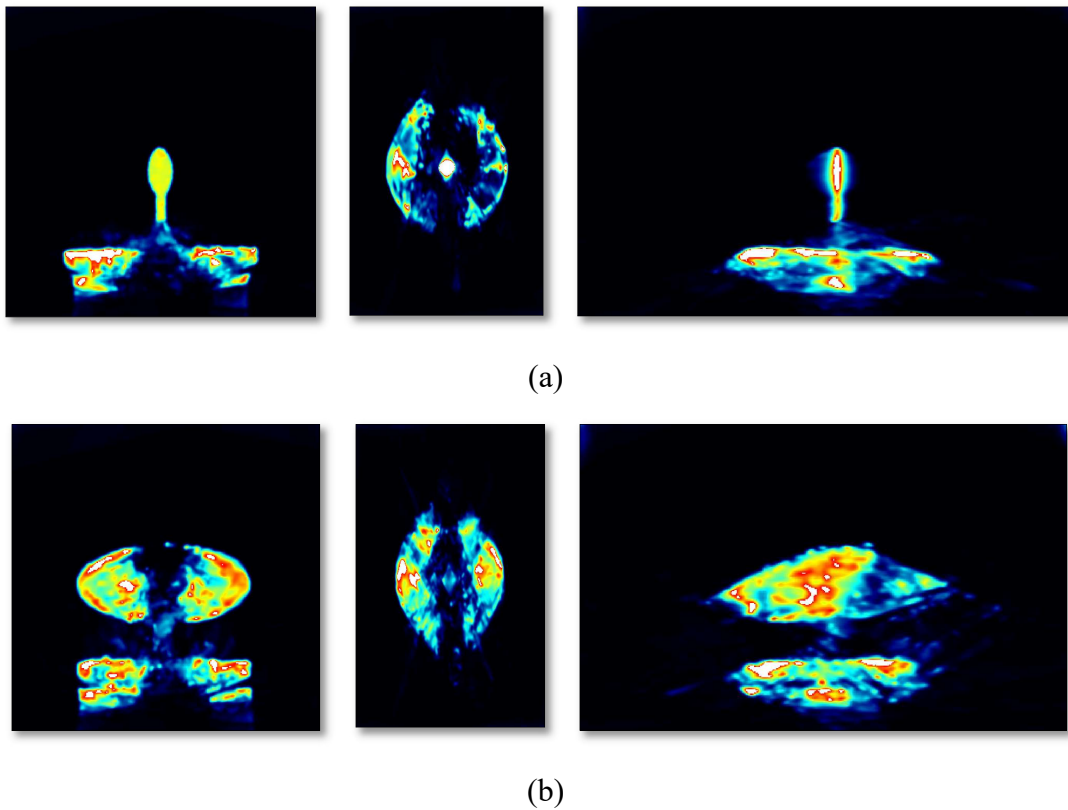
Figure 36. Reconstructions for all three planes for the 180° 4 inches orientation for (a) a small vertical spheroid, and (b) a large horizontal spheroid

It was also observed that the percentage error with respect to object size is smaller for larger objects as compared to smaller objects and the effect of angular separation evidently affects the reconstruction of larger objects more than smaller objects.

The effect of object size on reconstruction has been illustrated by Figure 37 (YZ plane – most error) and Figure 38 (XY plane – least error) for the 90° 7.5-inch orientation. Table 4 compares the absolute error computed from all three projections of the 90° 7.5-inch orientation.
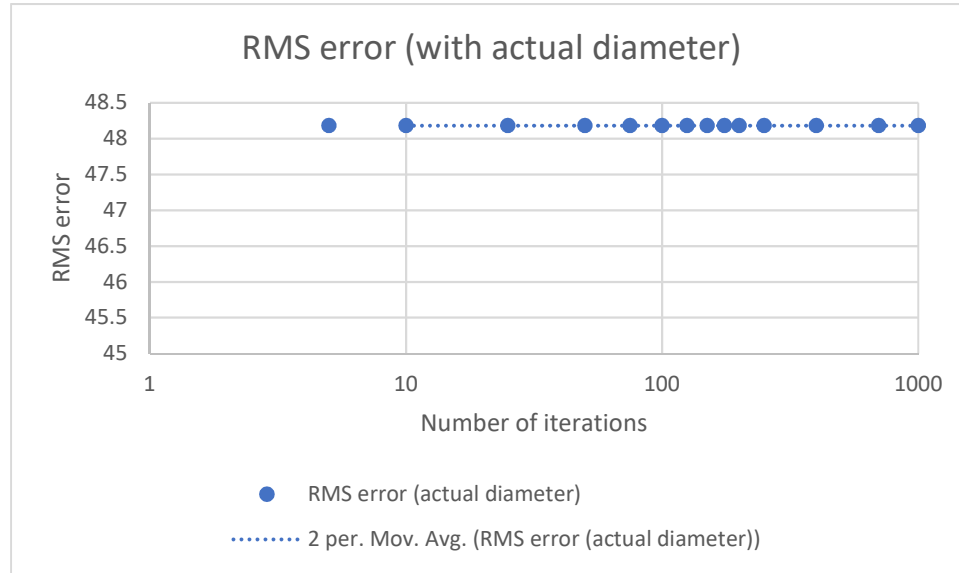
(a)
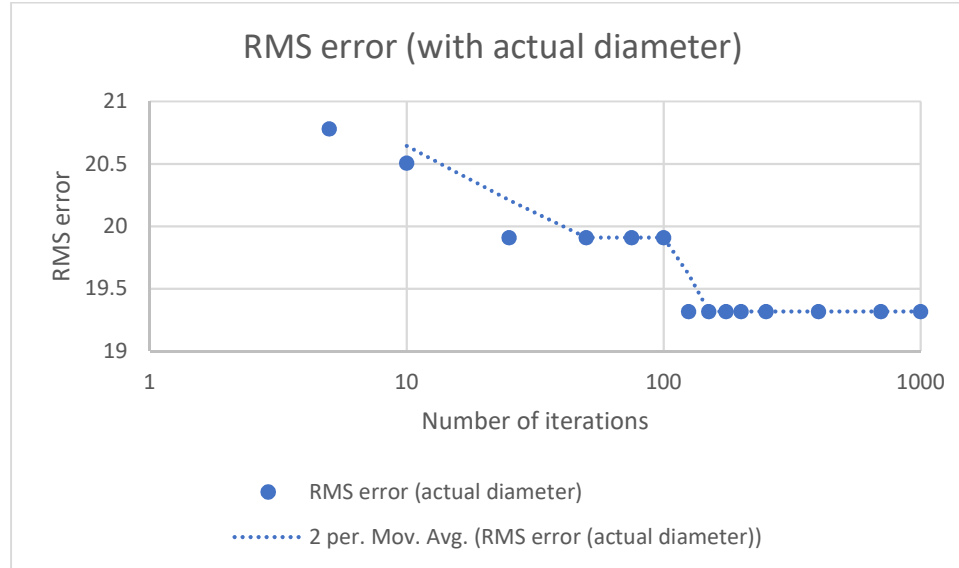
(b)

Figure 37. Error in reconstruction for the YZ plane for the 90° 7.5-inch orientation with boundary at 1% maximum intensity (a) 3 mm sphere reconstruction; (b) 10 mm sphere reconstruction
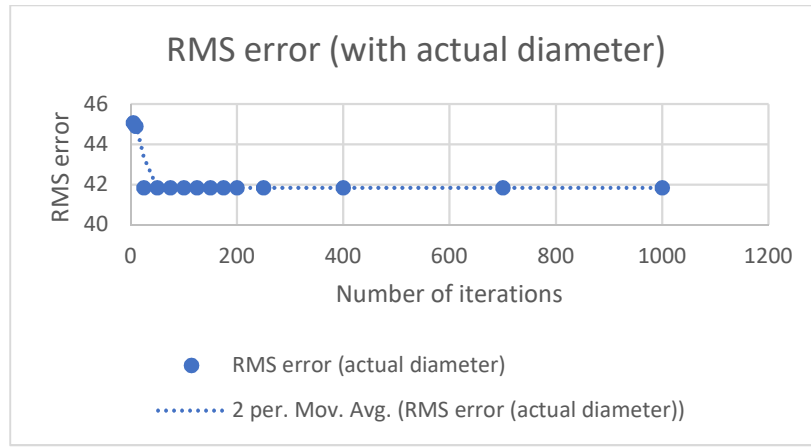
(a)
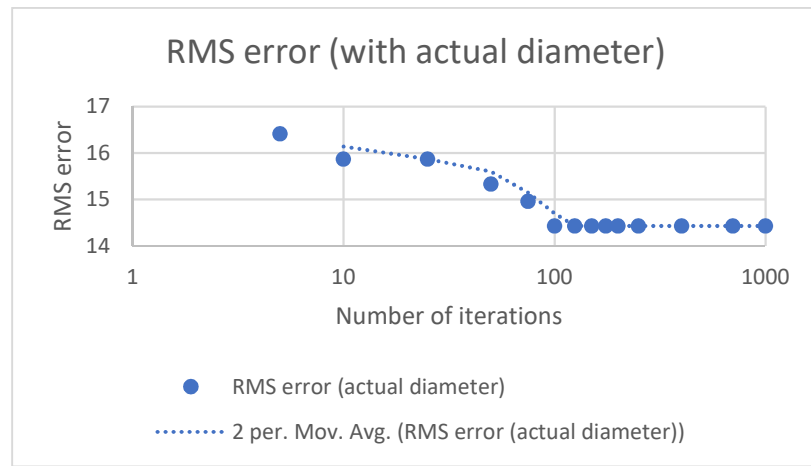
(b)

Figure 38. Error in reconstruction for the XY plane for the 90° 7.5- inch orientation with boundary at 1% maximum intensity (a) 3 mm sphere reconstruction; (b) 10 mm sphere reconstruction

Table 4. Comparison of absolute root mean square error (%) for different orientations and separation distances for the 3mm and 10mm diameter spherical target with boundary at 1% maximum intensity

ORIENTATION	3 MM SPHERE	10 MM SPHERE
90° 7.5 INCHES ARRANGEMENT	47.1 %	18.3 %
180° 4 INCHES ARRANGEMENT	51.9 %	34.3 %
180° 7.5 INCHES ARRANGEMENT	56.0 %	33.3 %

3.2.5 Object Material

Reconstructions were performed for targets made with both clear resin, analogous to semi-transparent fields, as well as flexible grey resin, analogous to opaque particles. The hypothesis is that the transparent targets would be easier to reconstruct than opaque targets.

It was observed that for the clear resin targets, even though uniform illumination is not achieved, sufficient light passes through the object such that internal features may also be captured. For the flexible grey resin targets, however, uniform illumination was very hard to achieve as the light does not pass through these objects. This made the visualization of internal features near to impossible.

In addition to this, non-convex opaque targets, for instance cubes, were seen to display shadowing effects, wherein no or very little light illuminates a certain surface leading to complete loss of information from that region. This effect occurs due to the inherent nature of opaque objects to block all light incident on it. The effect of shadowing is depicted in Figure 39.

Opaque targets were also observed to require more iterations to converge to a solution as compared to semi-transparent targets. A sample reconstruction for a combination of cubes is compared for both clear and flexible grey resin in Figure 40.

The effect of inadequate lighting on opaque targets may also be seen for large convex structures as illustrated in Figure 41.

(a)   (b)
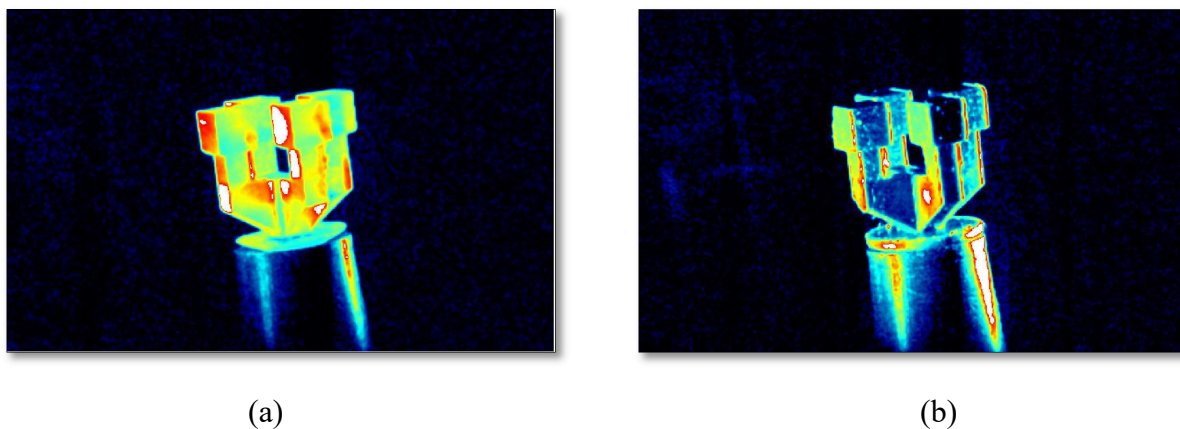
Figure 39. Effect of object material (a) Non-uniform but through illumination of semi-transparent object; (b) Shadowing effect for similar opaque object
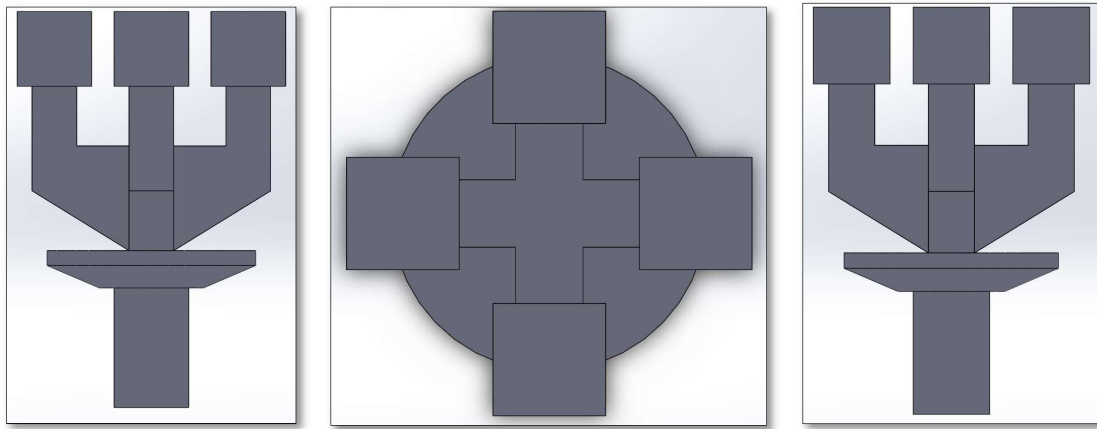
(a)
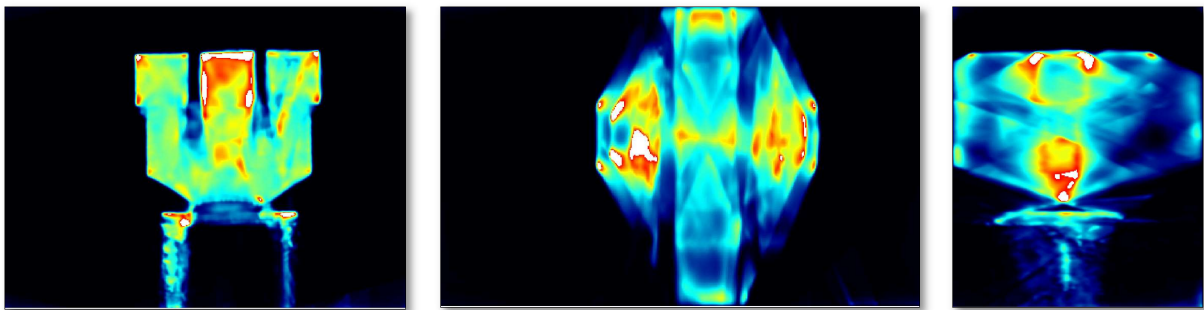
(b)
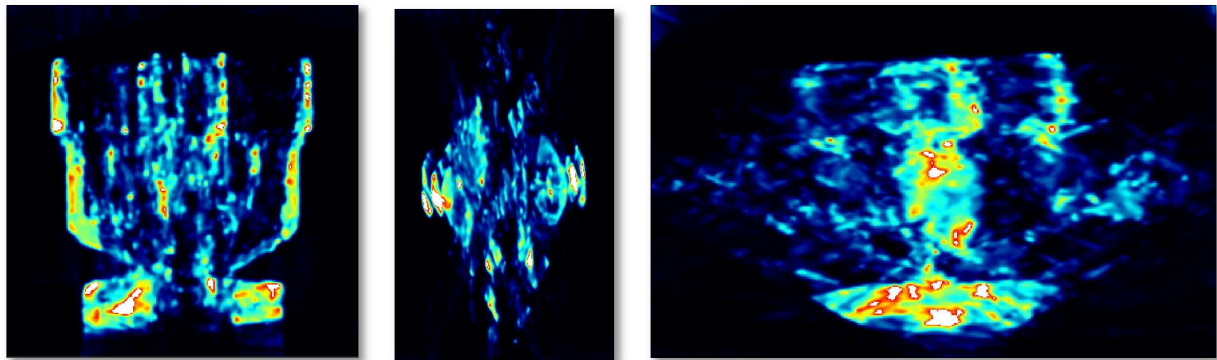
(c)

Figure 40. Effect of opacity for the 180° 4 inches orientation (a) Designed CAD model views for a cube combination; (b) Reconstructed clear image; (c) Reconstructed opaque image
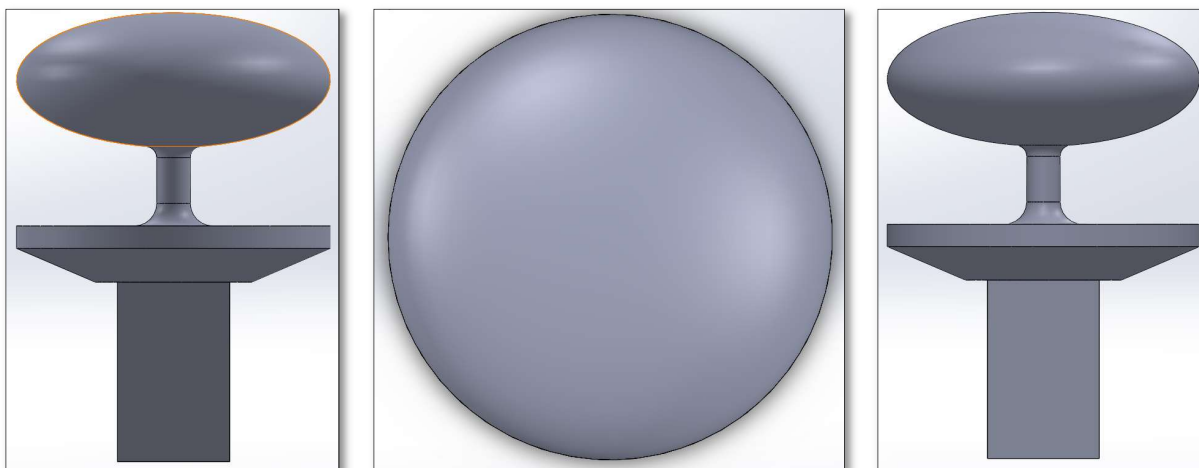
(a)
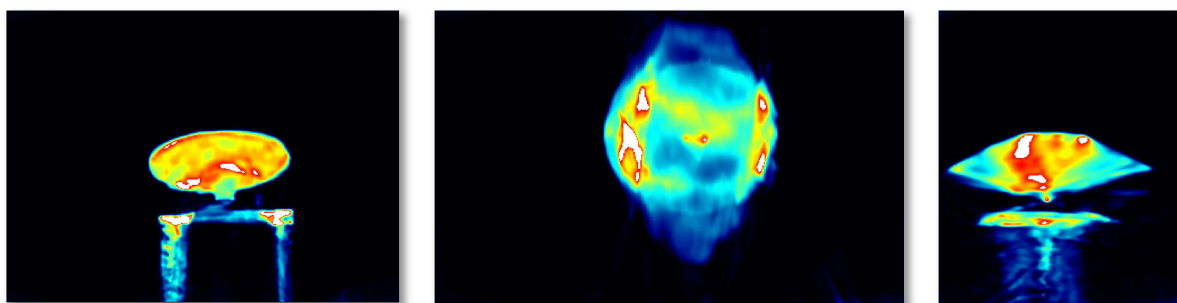
(b)
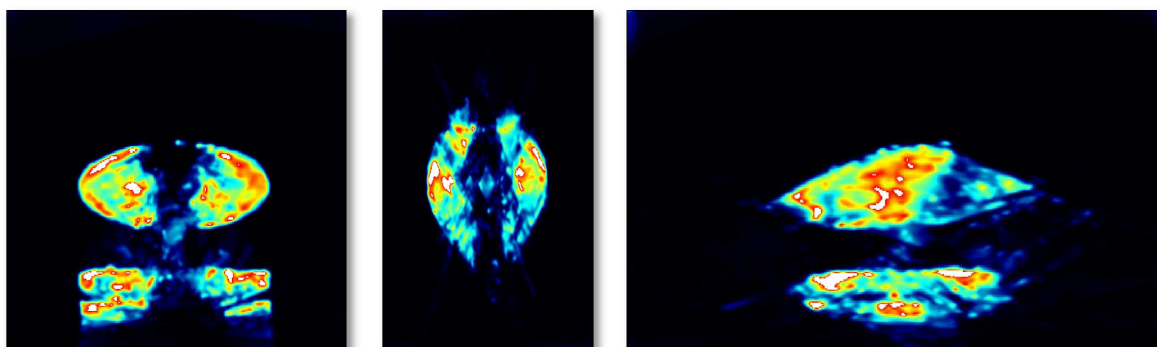
(c)

Figure 41. Effect of opacity for the 180° 4 inches orientation (a) Designed CAD model views for a spheroid; (b) Reconstructed clear image; (c) Reconstructed opaque image

3.2.6 Number of Views

It is expected that higher number of views result in better reconstructions. Trials were conducted to see the effect of number of views on reconstruction quality, including if information regarding the top and bottom views or side views is essential for good reconstructions.

For the first case, only the two views for each camera that captured the side views of the target were considered. The resultant reconstruction was seen to have a well reconstructed side view (YZ plane) projection with slight stretching that was not visible with the consideration of all eight views. The stretching is much more evident in the top view (XZ plane) which deviates considerably from a circle, which the projection should actually have resembled. Hence, the top view seems to be important in the case of closed figures like the targets under study.

The second trial comprised using only the top and bottom images from both quadscopes. This gave terrible reconstructions in the side view but a more circular top view closer to the solution from all eight views. Hence, the need for the captured side views is evident.

The next trial was conducted by using all the side views as well as the two top views, giving a total of six views. The reconstruction here seemed to match that using all eight views, indicating that the bottom view may not hold as much relevance to the current targets under study. Figure 42 details all the above-mentioned trials as well as the final reconstruction using all eight views.
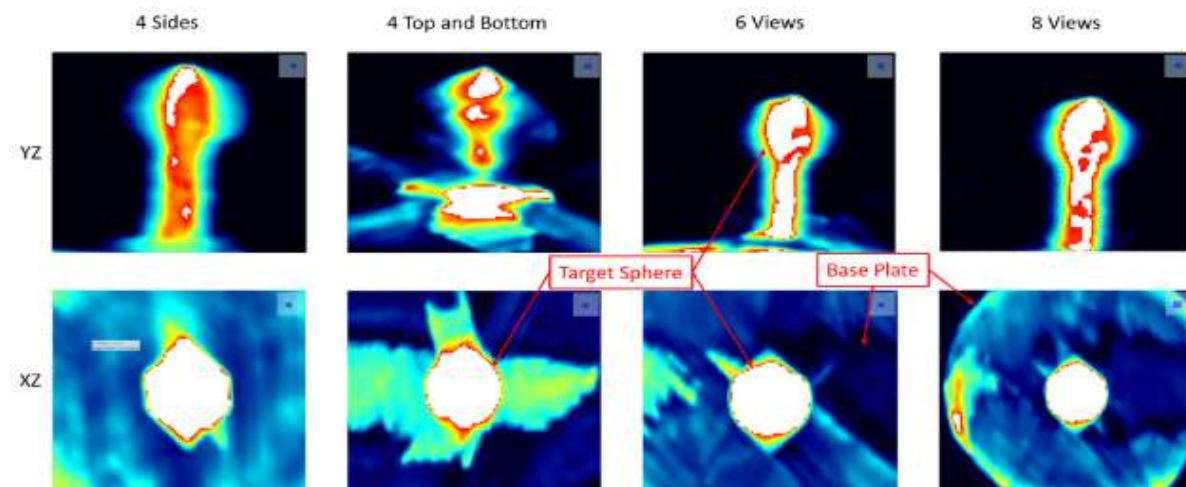
Figure 42. Projected YZ and XZ planar views for a spherical target for a 135° angular separation and 4-inch separation distance for different number of views

Trials were also done to compare the effect of using four views (a single camera, all side views or all top and bottom views), six views (four images from one camera and two from the other, or both top and bottom views with furthest side views), and finally all eight views.

It was observed that orientation played a big role in the effect of number of views. However, it was confirmed that using a combination of top and bottom views in conjunction with the two furthest apart side views gave a reconstruction almost equivalent to that of using all eight views. The effect of each of these trials is shown in Figure 43 and Figure 44.

(a)

(b)

(c)
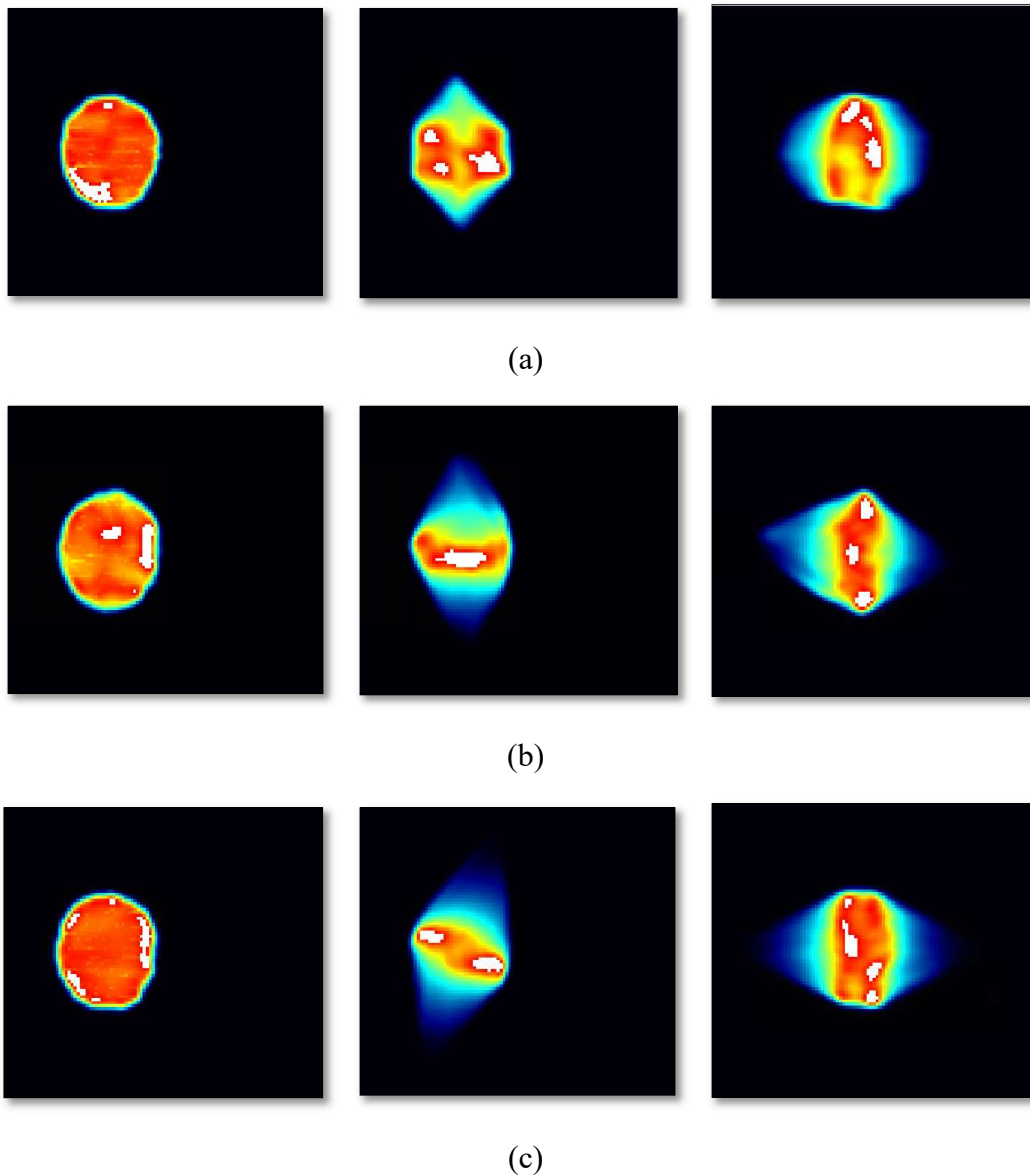
Figure 43. Reconstructions using four views (135° orientation) (a) Side views; (b) Top and bottom views; (c) One camera
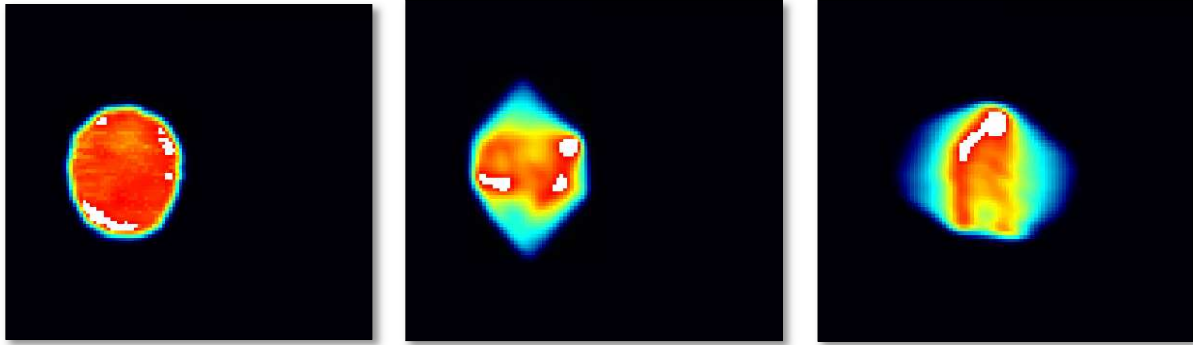
(a)
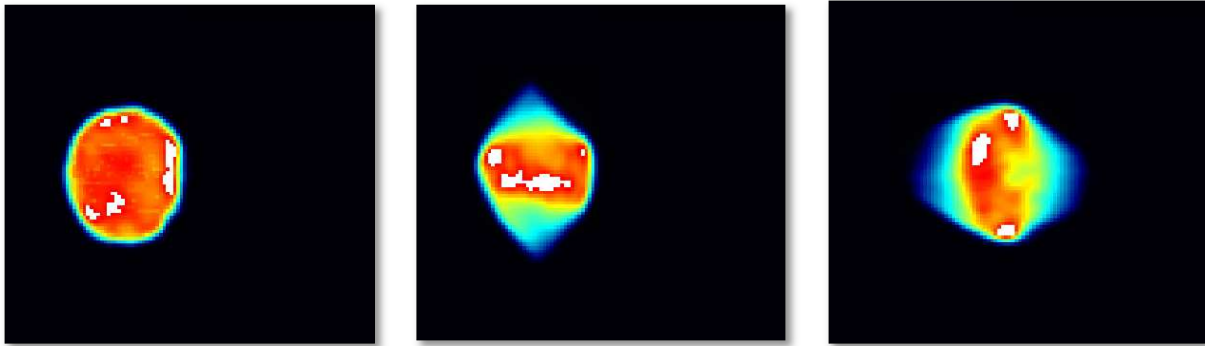
(b)
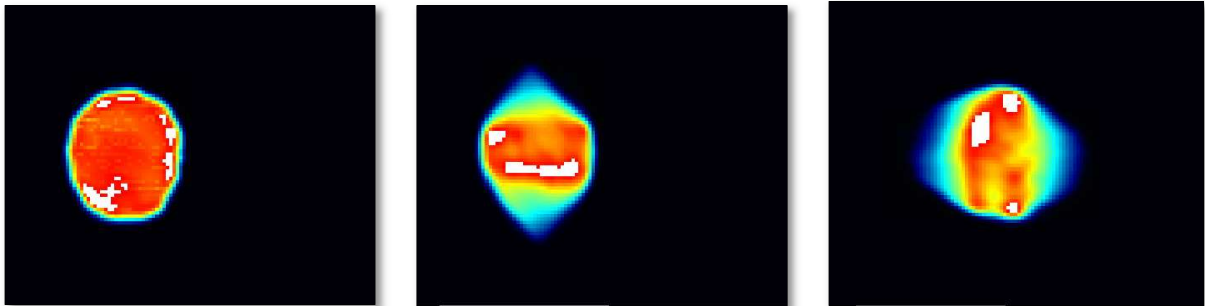
(c)

Figure 44. Reconstructions using two quadscopes (135° orientation) (a) Four views from one camera and two from the other; (b) Top, bottom and furthest side views from both cameras; (c) All eight views

Table 5 compares the error computed for the different number of views. It is seen that there is about 10% reduction in rms error with the use of a second quadscope (see results for single quadscope (camera 1 or 2) as opposed to two quadscopes (4 + 4)). Also, increase in the number of side views helps to improve reconstruction quality.

Table 5. Comparison of rms error for different number of views for the 135° 4 inches orientation at 1% of maximum intensity after 200 iterations

NUMBER OF VIEWS	RMS ERROR (%)
CAMERA 1	46.7
CAMERA 2	41.7
SIDE	34.7
TOP-BOTTOM	43.3
2 + 4	33.3
3 + 3	32.7
4 + 2	33.3
4 + 4	32.9

4. SUMMARY AND CONCLUSIONS

This thesis focused on the analysis of the accuracy of a Wide-Angle Relay Plenoptic (WARP) imaging system for multiphase fields. For this purpose, multiphase fields were emulated using some simple as well as complex geometries which were modelled in SolidWorks. The objects were 3D printed in clear resin as well as flexible grey resin to accommodate fields that are either semi-transparent, like sprays, or opaque, for instance solid particles in flow. A quadscope was built with a unique arrangement of four mirrors and four prisms such that each camera received four images instead of just one. Two such quadscopes were used in conjugation with two cameras to obtain eight views of the target under study. Light scattering from LEDs was used to illuminate the objects. The images were then processed using DaVis10 software with the help of the inbuilt MART reconstruction algorithm. A custom MATLAB code was developed and used to quantitatively analyze the quality of the reconstructed images.

The effect of varying different aspects of the imaging system as well as the target field was studied. The first parameter to be varied was the number of MART iterations performed. It was found that with an increase in number of iterations, the error with respect to the true solution reduced until finally converging to a stable value.

With increasing angular separation between the two cameras, more depth information was lost resulting in increased error. Interior features were reconstructed better in the 135° orientation as compared to the 180° orientation. The 90° orientation showed an inability to locate internal features spatially, but this is attributed to the fact that calibration incapabilities limit the number of useful views to six, with the two extreme side views being the ones eliminated.

It was observed that varying the separation distance between the target and the imaging system also affected the reconstruction quality, however the effect is highly dependent on the angular separation. As the angular separation increases, the effect of varying separation distance reduces.

With an increase in size of the object, it was seen that the percentage error with respect to actual solution decreases. It was also observed that the number of MART iterations required for the convergence of the reconstruction of smaller objects was considerably lower than that required for larger objects. Change in angular separation also has a greater effect on the reconstruction of larger objects as compared to smaller objects.

The reconstruction of clear objects was also compared to that of opaque objects. It was seen that non-convex opaque objects were greatly affected by shadowing effects due to their very nature. It was also observed that larger opaque objects were more difficult to reconstruct as light cannot pass through the entire object. Both these effects result in complete loss of vital field information due to absence of adequate lighting. Internal features of the field could not be reconstructed well due to the opacity. Good reconstructions could be obtained for the internal features of the semi-transparent objects as the light was able to pass through them completely. However, some reduction in intensity was visible, giving a non-uniform intensity field.

Finally, the effect of number of camera views on the reconstructed object was studied. For this, reconstructing with four views (using only four side views, using only two top and two bottom views, or using a single quadscope-camera combination), six views (using four views from one quadscope-camera pair and two from the other, or using two top and two bottom views in conjunction with the furthest side views), and finally all eight views were tested. It was observed that the use of two quadscopes (eight views) improved the reconstruction quality by about 10% as compared to using a single quadscope. The importance of the two extreme side views is also evident, which supports the claim that with increased calibration capabilities, the 90° configuration would result in even better reconstruction quality.

Hence, it is proposed that the 90° orientation with the least possible separation distance would be the best orientation for tomographic reconstruction studies for multiphase fields. However, until the calibration difficulties are resolved, an intermediate angle between the 135° and 90° may prove to be the best.

The quantitative studies detailed in this thesis have also brought to light some caveats in the setup. DaVis software requires the use of coplanar cameras for the best reconstruction. However, the very design of the setup is, by definition, non-coplanar. The importance of using multiple lighting sources or some means for uniform illumination is also evident. The need for background images for better background subtraction and noise reduction is also evident.

5. FUTURE WORK

There are several aspects of this system that may be worked on for both future developments as well its application in various multiphase fields. The first step would be to get a better estimate of the accuracy of the system in the imaging of multiphase fields through repeating the analysis with the use of multiple illumination sources such that problems like shadowing may be eliminated. The use of a calibration plate capable of simultaneously calibrating all eight views from a 90° orientation would help to expand and provide a more complete evaluation of the work done so far. It would also be worthwhile to perform reconstructions with angular separations between 90° and 135° where the calibration would be possible with the current calibration plate while ensuring that the reconstruction error is lower than that at 135°.

The current study used 3D objects printed in clear resin and flexible grey resin and used light scattering off of these objects to study the evaluation of the target. An alternative to ensure uniform lighting might be the use of a fluorescing material to 3D print the object. Fluorescent filaments as well as glow in the dark materials have been developed which can be infused into 3D printing filament which would ensure fluorescent targets and eliminate the need for external illumination.

Most fields that will be imaged would have features that fall into a smaller range of sizes than that studied here. As it was observed that the size of the object plays an important role in determining the effect of angular orientation on reconstruction quality, there seems to be a need to image smaller particles to see the effect of varying the different parameters on the same. For this, it may be worthwhile to study the flow of steady drops from a droplet generator. With a controlled system and a known drop size, quantitative measurements of the same would be possible using the current imaging system. As it has been seen that the use of shorter separation distances results in better reconstructions, it may be attempted to rebuild the quadscope and redesign it such that this distance may be reduced beyond 4 inches which is the current limit for the same.

While current error determination has been limited to the error in the XY, YZ and XZ planes, more information regarding the effect of the orientations and how they affect reconstructions might be obtained by studying the error at more angles, say 0° - 180° about the vertical axis and 0° - 90° about the horizontal axis.

It may also be worthwhile to recreate or expand on some pre-established work. The setting up of the experiment is underway to recreate the setup for the work by Halls *et al* [63] for using quadscopes for impinging spray visualization. The use of light scattering or fluorescent imaging using fluorescent tracers in the flowing water instead of X-ray imaging may be used to recreate this system and study the efficiency of this imaging system. Similarly, the work of Douglawi *et al* [36] may be expanded for 3D droplet evaporation imaging with the help of the two-quadscope setup.

Finally, prior work using a single quadscope for tomographic imaging of blasts may be extended to eight views using two quadscopes [7]. This seems to hold promise as it was shown that increasing the number of views to eight helped improve reconstruction quality.

REFERENCES

[1]   C. E. Brennen, *Fundamentals of Multiphase Flows*. 2005.

[2]   T. R. Meyer, B. R. Halls, N. Jiang, M. N. Slipchenko, S. Roy, and J. R. Gord, "High-speed, three-dimensional tomographic laser-induced incandescence imaging of soot volume fraction in turbulent flames," *Opt. Express*, vol. 24, no. 26, p. 29547, Dec. 2016, doi: 10.1364/oe.24.029547.

[3]   W. B. Ng and Y. Zhang, "Stereoscopic imaging and reconstruction of the 3D geometry of flame surfaces," *Exp. Fluids*, vol. 344, pp. 4484–493, 2003, doi: 10.1007/s00348-002-0585-6.

[4]   T. L. Medford *et al.*, "Stereoscopic planar laser-induced fluorescence imaging at 500 kHz," in *49th AIAA Aerospace Sciences Meeting Including the New Horizons Forum and Aerospace Exposition*, 2011, Accessed: May 02, 2020. [Online]. Available: https://ntrs.nasa.gov/search.jsp?R=20110003633.

[5]   B. R. Halls, P. S. Hsu, S. Roy, T. R. Meyer, and J. R. Gord, "Two-color volumetric laser-induced fluorescence for 3D OH and temperature fields in turbulent reacting flows," *Opt. Lett.*, vol. 43, no. 12, pp. 2961–2964, Jun. 2018, doi: 10.1364/OL.43.002961.

[6]   B. R. Halls, J. R. Gord, P. Hsu, S. Roy, and T. R. Meyer, "Development of two-color 3D tomographic VLIF measurements," *AIAA Aerosp. Sci. Meet. 2018*, no. 210059, pp. 2–7, 2018, doi: 10.2514/6.2018-1022.

[7]   D. K. Lauriola, M. Gomez, T. R. Meyer, S. F. Son, M. N. Slipchenko, and S. Roy, "High-speed particle image velocimetry and particle tracking methods in reactive and non-reactive flows," *AIAA Scitech 2019 Forum*, no. January, pp. 1–7, 2019, doi: 10.2514/6.2019-1605.

[8]   A. Faghri and Y. Zhang, *Transport Phenomena in Multiphase Systems*. Elsevier Science, 2006.

[9]   A. H. Lefebvre and V. G. McDonell, *Atomization and sprays*, Second edi. Combustion (New York, N.Y. : 1989), 2017.

[10]   T. R. Meyer, M. Brear, S. H. Jin, and J. R. Gord, "Formation and Diagnostics of Sprays in Combustion," in *Handbook of Combustion*, Weinheim, Germany: Wiley-VCH Verlag GmbH & Co. KGaA, 2010, pp. 291–322.

[11] D. R. Guildenbecher, C. López-Rivera, and P. E. Sojka, "Secondary atomization," *Exp. Fluids*, vol. 46, no. 3, pp. 371–402, Mar. 2009, doi: 10.1007/s00348-008-0593-2.

[12] D. G. Gordon, "Mechanism and speed of breakup of drops," *J. Appl. Phys.*, vol. 30, no. 11, pp. 1759–1761, 1959.

[13] A. C. Merrington and E. G. Richardson, "The breakup of liquid jets," *Proc. Phys. Soc. Lond.*, vol. 59, no. 331, pp. 1–13, 1947.

[14] J. L. York, H. F. Stubbs, and M. R. Tek, "The mechanism of disintegration of liquid sheets," *Trans. ASME*, vol. 75, pp. 1279–1286, 1953.

[15] Y. Mishra, "Droplet size, concentration, and temperature mapping in sprays using SLIPI-based techniques," 2018.

[16] S. C. Li, *Cavitation of Hydraulic Machinery*, vol. 1. PUBLISHED BY IMPERIAL COLLEGE PRESS AND DISTRIBUTED BY WORLD SCIENTIFIC PUBLISHING CO., 2000.

[17] F. Avellan, "Introduction to cavitation in hydraulic machinery," *6th Int. Conf. Hydraul. Mach. Hydrodyn.*, pp. 11–22, 2004, [Online]. Available: http://mmut.mec.upt.ro/mh/Conferinta_MH/102Avellan.pdf.

[18] M. Sommerfeld and H. H. Qiu, "Experimental studies of spray evaporation in turbulent flow," *Int. J. Heat Fluid Flow*, vol. 19, no. 1, pp. 10–22, Feb. 1998, doi: 10.1016/S0142-727X(97)10002-9.

[19] G. L. Hubbard, V. E. Denny, and A. F. Mills, "Droplet evaporation: Effects of transients and variable properties," *Int. J. Heat Mass Transf.*, vol. 18, no. 9, pp. 1003–1008, Sep. 1975, doi: 10.1016/0017-9310(75)90217-3.

[20] A. Douglawi, V. Athmanathan, M. N. Slipchenko, J. R. Gord, and T. R. Meyer, "Lifetime-filtered laser-induced exciplex fluorescence for crosstalk-free liquid-vapor imaging," *Opt. Lett.*, vol. 44, no. 6, p. 1402, Mar. 2019, doi: 10.1364/ol.44.001399.

[21] D. Zang, S. Tarafdar, Y. Y. Tarasevich, M. Dutta Choudhury, and T. Dutta, "Evaporation of a Droplet: From physics to applications," *Physics Reports*, vol. 804. Elsevier B.V., pp. 1–56, Apr. 29, 2019, doi: 10.1016/j.physrep.2019.01.008.

[22] C. K. Westbrook, "Chemical kinetics of hydrocarbon ignition in practical combustion systems," *Proc. Combust. Inst.*, vol. 28, pp. 1563–1577, 2000, doi: 10.1016/s0082-0784(00)80554-8.

[23]   C. K. Westbrook and W. J. Pitz, "A Comprehensive Chemical Kinetic Reaction Mechanism for Oxidation and Pyrolysis of Propane and Propene," *Combust. Sci. Technol.*, vol. 37, pp. 117–152, 1984.

[24]   J. Cavanagh, R. A. Cox, and G. Olson, "Computer modeling of cool flames and ignition of acetaldehyde," *Combust. Flame*, vol. 82, no. 1, pp. 15–39, 1990, doi: 10.1016/0010-2180(90)90075-3.

[25]   A. G. Gaydon and N. P. W. Moore, "Spectra of cool flames and pre-ignition glows," *Proc. R. Soc. London. Ser. A. Math. Phys. Sci.*, vol. 233, no. 1193, pp. 184–194, 1955, doi: 10.1098/rspa.1955.0254.

[26]   B. R. Halls, N. Jiang, T. R. Meyer, S. Roy, M. N. Slipchenko, and J. R. Gord, "4D spatiotemporal evolution of combustion intermediates in turbulent flames using burst-mode volumetric laser-induced fluorescence," *Opt. Lett.*, vol. 42, no. 14, pp. 2830–2833, Jul. 2017, doi: 10.1364/OL.42.002830.

[27]   B. R. Halls, J. R. Gord, N. Jiang, M. Splichenko, S. Roy, and T. R. Meyer, "High-speed three-dimensional tomographic measurements for combustion systems," in *32nd AIAA Aerodynamic Measurement Technology and Ground Testing Conference*, Jun. 2016, pp. 1–6, doi: 10.2514/6.2016-4027.

[28]   C. M. Jenkins, Y. Horie, and C. Y. Wu, "Particle velocity and structures in blast waves imaged using particle image velocimetry," *Int. J. Multiph. Flow*, vol. 36, no. 1, pp. 88–91, 2010, doi: 10.1016/j.ijmultiphaseflow.2009.08.004.

[29]   C. M. Jenkins, R. C. Ripley, C. Y. Wu, Y. Horie, K. Powers, and W. H. Wilson, "Explosively driven particle fields imaged using a high speed framing camera and particle image velocimetry," *Int. J. Multiph. Flow*, vol. 51, pp. 73–86, 2013, doi: 10.1016/j.ijmultiphaseflow.2012.08.008.

[30]   M. M. Biss, G. S. Settles, M. J. Hargather, L. J. Dodson, and J. D. Miller, "High-speed digital shadowgraphy of shock waves from explosions and gunshots," *Shock Waves*, vol. 16802, pp. 91–96, 2009, doi: 10.1007/978-3-540-85168-4_13.

[31]   L. A. Melton, "Spectrally separated fluorescence emissions for diesel fuel droplets and vapor," *Appl. Opt.*, vol. 22, no. 14, p. 2224, Jul. 1983, doi: 10.1364/ao.22.002224.

[32] J. Senda, M. Kobayashi, Y. Tanabe, and H. Fujimoto, "Quantitative Analysis of Fuel Vapor Concentration in Diesel Spray by Exciplex Fluorescence Method," *Vis. Quant. Anal. fuel Vap. Conc. diesel spray*, vol. 15, no. 2, pp. 149–156, 1994.

[33] M. Tsue, H. Hattori, A. Saito, and T. Kadota, "Planar Fluorescence Technique for Visualization of a Diesel Spray," *SAE Tech. Pap. 922205*, 1992, doi: https://doi.org/10.4271/922205.

[34] J. Yeom, T. Tanaka, J. Senda, and H. Fujimoto, "The Structure Analysis of Evaporative Diesel Spray," *SAE Tech. Pap. 2002-01-0498*, 2002, doi: https://doi.org/10.4271/2002-01-0498.

[35] A. Douglawi *et al.*, "Tracer-free liquid–vapor imaging using lifetime-filtered planar laser-induced fluorescence," *Opt. Lett.*, vol. 44, no. 8, p. 2101, Apr. 2019, doi: 10.1364/ol.44.002101.

[36] A. Douglawi, "Liquid-Vapor Imaging in Fuel Sprays using Lifetime-Filtered Planar Laser-Induced Fluorescence," 2018.

[37] B. D. Ritchie and J. M. Seitzman, "Simultaneous imaging of vapor and liquid spray concentration using combined acetone fluorescence and phosphorescence," in *AIAA Paper*, 2004, pp. 161–168, doi: 10.2514/6.2004-384.

[38] M. R. Herfatmanesh, M. A. Attar, and H. Zhao, "Simultaneous imaging of diesel spray atomisation and evaporation processes in a single-cylinder CR diesel engine," *Exp. Therm. Fluid Sci*, vol. 50, pp. 10–20, 2013, doi: d10.1016/j.expthermflusci.2013.04.019.

[39] Y. Wu, W. Xu, Q. Lei, and L. Ma, "Single-shot volumetric laser induced fluorescence (VLIF) measurements in turbulent flows seeded with iodine," *Opt. Express*, vol. 23, no. 26, pp. 33408–33418, 2015, doi: 10.1364/OE.23.033408.

[40] T. Li *et al.*, "Tomographic imaging of OH laser-induced fluorescence in laminar and turbulent jet flames Related content," *Meas. Sci. Technol.*, vol. 29, no. 1, p. 015206, 2018, doi: 10.1088/1361-6501/aa938a.

[41] O. L. Gülder, G. J. Smallwood, and D. R. Snelling, "Diesel Spray Structure Investigation by Laser Diffraction and Sheet Illumination," *SAE Pap. 920577*, 1992.

[42] H. Kosaka, Y. H. Won, and T. Kaminoto, "A Study of the Structure of Diesel Sprays Using 2-D Imaging Techniques," *SAE Pap. 920107*, vol. SAE Transa, pp. 175–186, 1992.

[43] M. H. Davy, P. A. Williams, and R. W. Anderson, "Effects of fuel composition on mixture formation in a firing direct-injection spark-ignition (DISI) engine: An experimental study using mie-scattering and planar laser-induced fluorescence (PLIF) techniques," in *SAE Technical Papers 2000-01-1904*, Jun. 2000, doi: 10.4271/2000-01-1904.

[44] T. R. Meyer, S. Roy, V. M. Belovich, E. Corporan, and J. R. Gord, "Simultaneous planar laser-induced incandescence, OH planar laser-induced fluorescence, and droplet Mie scattering in swirl-stabilized spray flames," *Appl. Opt.*, vol. 44, no. 3, pp. 445–454, 2005.

[45] Y. N. Mishra, E. Kristensson, and E. Berrocal, "Reliable LIF/Mie droplet sizing in sprays using structured laser illumination planar imaging," *Opt. Express*, vol. 22, no. 4, p. 4492, Feb. 2014, doi: 10.1364/oe.22.004480.

[46] E. Berrocal, E. Kristensson, M. Richter, M. Linne, and M. Aldén, "Application of Structured Illumination for Multiple Scattering Suppression in Planar Laser Imaging of Dense Sprays," *Opt. Express*, vol. 16, no. 22, pp. 17870–17881, Oct. 2008.

[47] R. J. H. Klein-Douwel, P. J. M. Frijters, L. M. T. Somers, W. A. de Boer, and R. S. G. Baert, "Macroscopic diesel fuel spray shadowgraphy using high speed digital imaging in a high pressure cell," *Fuel*, vol. 86, no. 12–13, pp. 1994–2007, Aug. 2007, doi: 10.1016/j.fuel.2006.11.039.

[48] D. R. Emberson, B. Ihracska, S. Imran, and A. Diez, "Optical characterization of Diesel and water emulsion fuel injection sprays using shadowgraphy," *Fuel*, vol. 172, pp. 253–262, May 2016, doi: 10.1016/j.fuel.2016.01.015.

[49] J. Klinner and C. Willert, "Tomographic shadowgraphy for three-dimensional reconstruction of instantaneous spray distributions," *Exp. Fluids*, vol. 53, no. 2, pp. 531–543, Aug. 2012, doi: 10.1007/s00348-012-1308-2.

[50] M. Linne, M. Paciaroni, T. Hall, and T. Parker, "Ballistic Imaging of the Near Field in a Diesel Spray," *Exp. Fluids*, vol. 40, pp. 836–846, 2006.

[51] J. B. Schmidt, Z. D. Schaefer, T. R. Meyer, S. Roy, S. A. Danczyk, and J. R. Gord, "Ultrafast time-gated ballistic-photon imaging and shadowgraphy in optically dense rocket sprays," *Appl. Opt.*, vol. 48, no. 4, p. B144, Feb. 2009, doi: 10.1364/ao.48.00b137.

[52] Z. U. Puayen Tan, K. Johnson, C. Clifford, and B. S. Thurow, "Development of a modular, high-speed plenoptic-camera for 3D flow-measurement," *Opt. Express*, vol. 27, no. 9, pp. 13400–13415, Apr. 2019, doi: 10.1364/OE.27.013400.

[53] Z. P. Tan, R. Alarcon, J. Allen, B. S. Thurow, and A. Moss, "Development of a high-speed plenoptic imaging system and its application to marine biology PIV," *Meas. Sci. Technol.*, vol. 31, p. 054005, 2020, doi: 10.1088/1361-6501/ab553c.

[54] P. M. Lillo, M. L. Greene, and V. Sick, "Plenoptic singleshot 3D imaging of in-cylinder fuel spray geometry," *Z. Phys. Chem.*, vol. 229, pp. 549–560, 2015.

[55] B. R. Halls *et al.*, "kHz-rate four-dimensional fluorescence tomography using an ultraviolet-tunable narrowband burst-mode optical parametric oscillator," *Optica*, vol. 4, no. 8, pp. 897–902, Aug. 2017, doi: 10.1364/OPTICA.4.000897.

[56] P. J. Santangelo and P. E. Sojka, "Focused-image holography as a dense-spray diagnostic," *Appl. Opt.*, vol. 33, no. 19, p. 4132, Jul. 1994, doi: 10.1364/ao.33.004132.

[57] J. Burke, C. F. Hess, and V. Kebbel, "Digital Holography for Instantaneous Spray Diagnostics on a Plane," *Part. Part. Syst. Charact.*, vol. 20, no. 3, pp. 183–192, Jun. 2003, doi: 10.1002/ppsc.200390024.

[58] F. Mayinger and A. Chávez, "Measurement of direct-contact condensation of pure saturated vapour on an injection spray by applying pulsed laser holography," *Int. J. Heat Mass Transf.*, vol. 35, no. 3, pp. 691–702, Mar. 1992, doi: 10.1016/0017-9310(92)90128-F.

[59] J. Muller, V. Kebbel, and W. Juptner, "Characterization of spatial particle distributions in a spray-forming process using digital holography," *Meas. Sci. Technol.*, vol. 15, pp. 706–710, 2004, doi: 10.1088/0957-0233/15/4/013.

[60] J. Gao, D. R. Guildenbecher, P. L. Reu, V. Kulkarni, P. E. Sojka, and J. Chen, "Quantitative, three-dimensional diagnostics of multiphase drop fragmentation via digital in-line holography," *Opt. Lett.*, vol. 38, no. 11, p. 1895, Jun. 2013, doi: 10.1364/ol.38.001893.

[61] D. R. Guildenbecher, J. Gao, J. Chen, and P. E. Sojka, "Characterization of drop aerodynamic fragmentation in the bag and sheet-thinning regimes by crossed-beam, two-view, digital in-line holography," *Int. J. Multiph. Flow*, vol. 94, pp. 107–122, 2017.

[62] T. J. Heindel Bergles, "A Review of X-Ray Flow Visualization With Applications to Multiphase Flows," *J. Fluids Eng.*, vol. 133, pp. 074001-1-074001–16, Jul. 2011, doi: 10.1115/1.4004367.

[63] B. R. Halls *et al.*, "4D spatiotemporal evolution of liquid spray using kilohertz-rate x-ray computed tomography," *Opt. Lett.*, vol. 44, no. 20, pp. 5013–5016, Oct. 2019, doi: 10.1364/OL.44.005013.

[64] T. R. Meyer, J. B. Schmidt, S. M. Nelson, J. B. Drake, D. M. Janvrin, and T. J. Heindel, "Three-Dimensional Spray Visualization using X-ray Computed Tomography," in *ILASS Americas, 21st Annual Conference on Liquid Atomization and Spray Systems*, May 2008.

[65] G. T. Herman, *Fundamentals of computerized tomography: Image reconstruction from projection*, 2nd editio. Springer, 2009.

[66] S. Ghaemi and F. Scarano, "Multi-pass light amplification for tomographic particle image velocimetry applications," *Meas. Sci. Technol.*, vol. 21, no. 12, p. 127002, 2010.

[67] J. Radon, "ON THE DETERMINATION OF FUNCTIONS FROM THEIR INTEGRAL VALUES ALONG CERTAIN MANIFOLDS," *IEEE Trans. Med. Imaging*, vol. MI–5, no. 4, pp. 170–176, Dec. 1986, doi: 10.1109/TMI.1986.4307775.

[68] R. Gordon, R. Bender, and G. T. Herman, "Algebraic Reconstruction Techniques (ART) for Three-dimensional Electron Microscopy and X-ray Photography," *J. theor. Biol.*, vol. 29, pp. 471–481, 1970.

[69] D. Mishra, K. Muralidhar, and P. Munshi, "A ROBUST MART ALGORITHM FOR TOMOGRAPHIC APPLICATIONS," *Numer. heat Transf.*, vol. 35, no. 4, pp. 485–506, 1999, doi: 10.1080/104077999275857.

[70] T. R. Meyer, B. R. Halls, N. Jiang, M. N. Slipchenko, S. Roy, and J. R. Gord, "High-speed, three-dimensional tomographic laser-induced incandescence imaging of soot volume fraction in turbulent flames," *Opt. Express*, vol. 24, no. 26, pp. 29547–29555, Dec. 2016, doi: 10.1364/oe.24.029547.

[71] S. Roy, N. Jiang, P. S. Hsu, and H. U. Stauffer, "4D imaging of fast flow dynamics: From challenging dream to reality," in *AIP Conference Proceedings*, 2019, vol. 2121, p. 20002, doi: 10.1063/1.5115843.